AGU PUBLICATIONS

JGR

Journal of Geophysical Research: Solid Earth

RESEARCH ARTICLE
10.1002/2014JB011850

Key Point:
- Most of the structure of a rift can be explained by repeated dike intrusions

Correspondence to:
D. Trippanera,
daniele.trippanera@uniroma3.it

Citation:
Trippanera, D., J. Ruch, V. Acocella, and E. Rivalta (2015), Experiments of dike-induced deformation: Insights on the long-term evolution of divergent plate boundaries, *J. Geophys. Res. Solid Earth*, *120*, doi:10.1002/2014JB011850.

Received 22 DEC 2014
Accepted 24 SEP 2015
Accepted article online 29 SEP 2015

Experiments of dike-induced deformation: Insights on the long-term evolution of divergent plate boundaries

D. Trippanera[1], J. Ruch[1,2], V. Acocella[1], and E. Rivalta[3]

[1]Science Department, Roma Tre University, Rome, Italy, [2]Now at Physical Science and Engineering Division, King Abdullah University of Science and Technology, Thuwal, Saudi Arabia, [3]Deutsches GeoForschungsZentrum Potsdam, Potsdam, Germany

Abstract The shallow transport of magma occurs through dikes causing surface deformation. Our understanding of the effects of diking at the surface is limited, especially on the long term, for repeated intrusive episodes. We use analogue models to study the upper crustal deformation induced by dikes. We insert metal plates within cohesive sand with three setups: in setup A, the intrusion rises upward with constant thickness and in setups B and C, the intrusion thickens at a fixed depth, with final rectangular (setup B) or triangular (setup C) shape in section. Setup A creates a doming delimited by reverse faults, with secondary apical graben, without close correspondence in nature. In setups B and C, a depression flanked by two uplifted areas is bordered by inward dipping normal faults propagating downward and, for deeper intrusions in setup B, also by inner faults, reverse at the surface; this deformation is similar to what is observed in nature, suggesting a consistent physical behavior. Dikes in nature initially propagate developing a mode I fracture at the tip, subsequently thickened by magma intrusion, without any host rock translation in the propagation direction (as in setup A). The deformation pattern in setups B and C depends on the intrusion depth and thickness, consistently to what is observed along divergent plate boundaries. The early deformation in setups B and C is similar to that from a single rifting episode (i.e., Lakagigar, Iceland, and Dabbahu, Afar), whereas the late stages resemble the structure of mature rifts (i.e., Krafla, Iceland), confirming diking as a major process in shaping divergent plate boundaries.

1. Introduction

The shallow transport of magma, including that feeding most eruptions, occurs by means of dikes. Dikes play a fundamental role in controlling the magmatic, structural, and morphological evolution of volcanic edifices by feeding their rift zones [i.e., *Swanson et al.*, 1976; *Pollard et al.*, 1983; *Acocella and Neri*, 2009]. At a larger scale, dikes have been proposed to control the evolution of divergent plate boundaries by directly generating rifting episodes which represent the culmination of a regional tectonic process of plate spreading [i.e., *Bjornsson et al.*, 1977; *Opheim and Gudmundsson*, 1989; *Rubin*, 1992; *Buck et al.*, 2006; *Wright et al.*, 2006; *Ebinger et al.*, 2010, and references therein]. In the last decades, geological, geodetic, and geophysical observations detected repeated rifting events (characterized by a dike emplaced in a few days) or episodes (several dikes emplaced in a few years) along divergent plate boundaries, in Iceland [*Krafla*, 1975–1984; *Bárðarbunga*, 2014, 2015; *Bjornsson et al.*, 1977; *Sigurdsson*, 1980; *Rubin and Pollard*, 1988; *Rubin*, 1992; *Sigmundsson et al.*, 2014], Tanzania [*Calais et al.*, 2008], and Afar [*Asal-Ghoubet* 1978; *Dallol*, 2004; *Dabbahu*, 2005–2009; *Ruegg et al.*, 1979; *Wright et al.*, 2006; *Nobile et al.*, 2012]. In the Dabbahu case, the *m*-scale reactivation of preexisting normal faults during dike injection has been directly witnessed [*Rowland et al.*, 2007], confirming that normal faults may be generated by dikes, possibly with an upward propagation [*Grant and Kattenhorn*, 2004; *Tentler*, 2005]. These studies lead to a general consensus that magma injection may be a primary factor affecting the activity and shape of the rift zones. At the surface, these rift zones usually consist of grabens, eruptive fissures, normal faults, and extension fractures. These are organized in magmatic systems, with a dominant volcano connected to along-rift fissure swarms. At depth, the analysis of the extinct and exhumed magmatic systems, as in Eastern Iceland, shows that these almost exclusively consist of dike swarms, locally reaching 5–10% of the crustal width. However, here the upper tips of the dikes are not connected to the bottom of any normal fault; indeed, normal faulting appears restricted to the uppermost crust and not geometrically connected to the underlying dike complex [i.e., *Gudmundsson*, 1983; *Forslund and Gudmundsson*, 1991; *Paquet et al.*, 2007]. Long-term strain

accumulation along plate boundaries may also enhance fault slip at the surface during inter-rifting episodes [*Calais et al.*, 2008; *Ebinger et al.*, 2010], possibly explaining a part of the observed deformation pattern at the surface and the lack of connection between the normal faults and the dike tips. Therefore, it is still unclear how much of the cumulative surface deformation observed along divergent plate boundaries or rift zones may be directly related to dike-induced rifting episodes or to regional strain inducing plate spreading. A major limitation in understanding the longer-term plate separation process is represented by the partial observation of its evolution, both at the surface and at depth. Geodesy commonly captures a single rifting episode or, seldom, inter-rifting deformation with a time scale ($1–10^1$ years) much shorter than that responsible for regional plate spreading. Conversely, structural field data commonly show the final, cumulative result of several rifting events and episodes ($10^4–10^5$ years). Therefore, any understanding of the processes in between, potentially characterized by variable amounts of tectonic and magmatic contributions, is poorly constrained.

In order to better understand the structural development of rift zones along divergent plate boundaries, we experimentally simulate progressive dike intrusions (i.e., incremental dike opening at a fixed depth) and analyze the resulting deformation. In particular, the key aspect we want to address is the study of the long-term (~10^2 to ~10^4 years) surface deformation resulting from repeated dike-induced rifting episodes. Our aim is to simulate this deformation in the experiments and then compare this with what is observed along magmatic divergent plate boundaries to better capture any long-term role of magmatism on the rift structure. For this, we performed a parametric study, where we mainly considered the depth to the top of the injections and their final thickness. Our qualitative comparison is mainly based on the occurrence of specific structural (geometric and kinematic) features, which may be otherwise difficult to reconcile with nonmagmatic (i.e., tectonic) processes alone. A few experimental studies have already analyzed the deformation pattern due to dike intrusion. Some experiments have been carried out intruding golden syrup or vegetable oil, as magma analogue, into granular materials, simulating the brittle crust. The results show a broad dome, bounded by reverse faults, above the dike [*Mathieu et al.*, 2008; *Abdelmalak et al.*, 2012]. However, this deformation pattern does not seem comparable with that observed at rift zones in nature, where a major subsiding area, bordered by inward dipping faults, forms above the dike [i.e., *Rubin and Pollard*, 1988; *Wright et al.*, 2006]. The deformation due to dike emplacement has also been studied intruding cards within a granular material, obtaining a fault-bounded depression above the intrusion, more consistent to natural cases [*Fink and Pollard*, 1983; *Mastin and Pollard*, 1988]. In this study, we use a derivate of the *Mastin and Pollard* [1988] setup as a proxy for our experiments. Despite the overall similar setup, we expect to better capture the surface deformation pattern through a more comprehensive parametric study and the use of techniques (including the particle image velocimetry (PIV) analysis, see below) to face a more detailed comparison to nature. In particular, the main differences with *Mastin and Pollard* [1988] are as follows: (a) *Mastin and Pollard* [1988] focus their analysis and interpretation on the inflation of a single dike, whereas we aim to simulate the growth of a dike swarm; (b) we test different modalities and shapes of intrusions, studying more in detail the effect of the intrusion depth and thickness and its geometry on both the structure of the deformation and the fault kinematics; (c) we use image correlation techniques and laser scanner acquisitions to monitor the deformation of the experiments, obtaining detailed deformation map and time series for both horizontal and vertical displacements; and (d) we use cohesive material made of homogeneous crushed silica sand (instead of a flour and sugar mixture with a corn meal layering) to simulate the host rock and metal plates for dike analogues.

More in general, our models provide a new approach compared to previous models, as we aim to understand the evolution of the deformation simulating multiple rifting episodes, in order to capture the long-term evolution of rift zones.

2. Experimental Setup and Scaling

2.1. Setup and Methods

The repeated emplacement of dikes and the development of a dike complex may be achieved in the experiments through two end-member processes: (a) the upward rise of the plate(s) inserted within the sand, maintaining the same thickness throughout the experiment, and (b) the thickening of the intrusion complex due to incremental insertion of each plate within a sleeve, maintaining a constant depth of insertion. In order to test both modes, we perform two series of experiments in which we simulate (a) upward propagating dikes with constant thickness (setup A) and (b) an incrementally thickening dike complex at a fixed depth (setups B and C). We maintain the

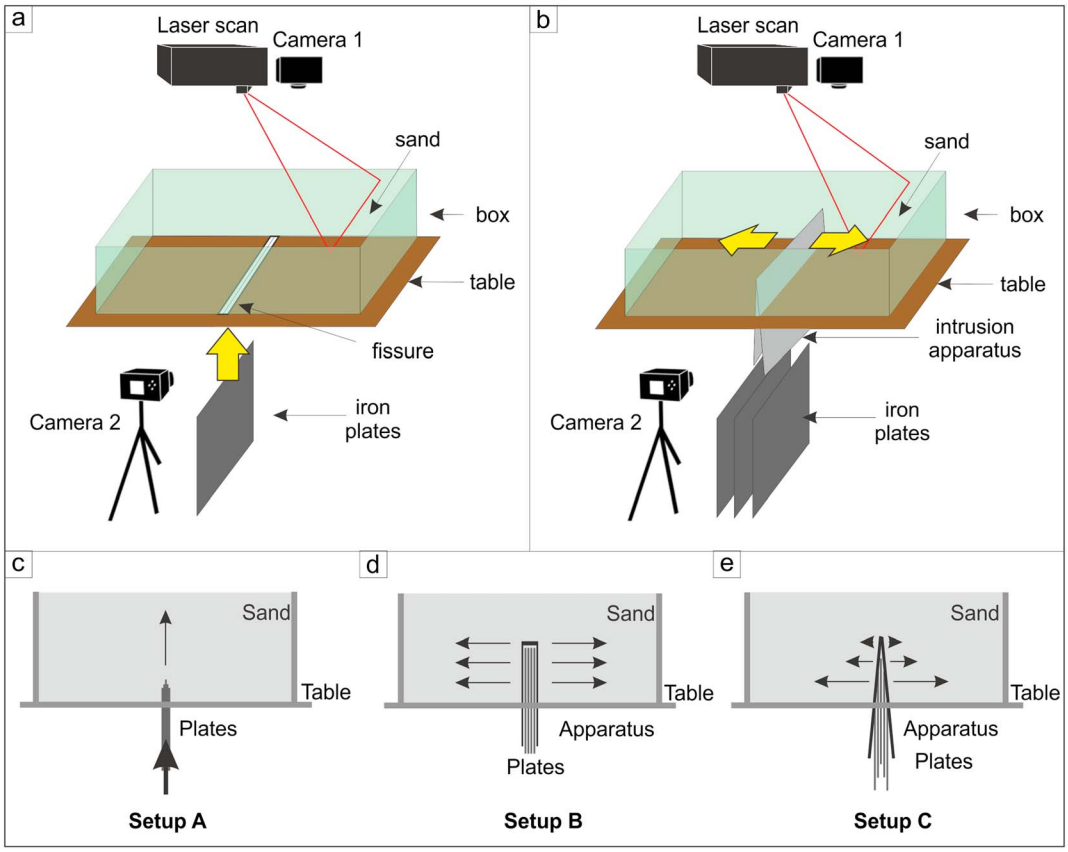

Figure 1. Scheme of the apparatus used for (a) the rising (setup A) and (b) the thickening intrusion models (setups B and C). The yellow arrows indicate the rise of the plates in Figure 1a and the thickening of the intrusions in Figure 1b. Schematic section view of setup (c) A, (d) B, and (e) C.

same boundary conditions for all the experiments, consisting of a glass box (25 × 45 × 15 cm) hosting a central vertical slot (25 × 2 cm) where the metal plates (dike analogues) are intruded. The box is filled with crushed silica sand, as upper crust analogue (see section 2.2). The incremental dike intrusion is simulated by the progressive vertical insertion of 20 × 20 cm iron plates, 0.5 mm thick, into the central slot (Figure 1).

In the models with upward propagating intrusions (setup A), the iron plates are directly inserted into the sand through the slot at the base of the sand box (Figures 1a and 1c). Each plate is pushed 2.5–3 cm upward into the sand by incremental steps of 0.5 cm. By using this setup, the overall initial intrusion thickness during the experiment is kept constant, while the upper tip of the intrusion propagates upward. In order to test how the intrusion thickness affects the results, we consider a total thickness of the analogue intrusions of 0.5 mm in model A1 (1 plate) and 2.5 mm in model A2 (5 plates; Table 1). For brevity, here we show only experiment A2.

In setups B and C, the intrusion depth is fixed and the intrusion thickens. These setups consist of intrusions of the analogue dikes through a vertical slot at fixed depth (6 cm from the base of the box). The slot is formed by two parallel and rigid Plexiglas sheets (25 × 25 cm) (Figure 1b) jointed on their top and allowed to move horizontally but not vertically. Therefore, the intrusion apparatus can only dilate at a fixed depth under the incremental injection of up to 20 metal plates (each 0.5 mm thick) into the slot. We also vary the final shape of the intrusion in section view, testing its influence on the deformation pattern. The junction at the top of the Plexiglas plates allows us to modify the final intrusion geometry and also to control the amount of opening at the top. In setup B, the top of the intrusion complex can dilate up to 1 cm, similar to its base (Table 1). In this case, the final shape of the intrusions has a rectangular shape in section view (Figure 1d). In setup C, the maximum dilation of the intrusion top is 0.2 cm, whereas the base can dilate up to 1 cm, providing an overall triangular shape of the intrusions in section view (Figure 1e and Table 1). In order to assess the influence of the intrusion depth, we perform six experiments with setup B and three with setup C, varying the intrusion depth from 1 cm to 8 cm. Here we describe three experiments with setup B and two with setup C (Table 1).

Table 1. List of the Experiments (First Column) and Relative Parameters[a]

Experiment	Setup	Type	Tip	Depth	Maximum Thickness	Faulting Thickness	
A1	A	rising			0.05 cm		
A2	A	rising			0.20 cm		
B1	B	opening	*R*	1 cm	1.00 cm	0.05 cm	
B2	B	opening	*R*	2 cm	1.00 cm	0.10 cm	
B3	B	opening	*R*	3 cm	1.00 cm	0.20 cm	
B4	B	opening	*R*	4 cm	1.00 cm	0.30 cm	
B5	B	opening	*R*	4 cm	1.00 cm	0.20 cm	asymmetric
B6	B	opening	*R*	8 cm	1.00 cm	0.60 cm	
C1	C	opening	*T*	2 cm	0.20 cm	0.05 cm	sand cone
C2	C	opening	*T*	4 cm	0.20 cm	0.10 cm	
C3	C	opening	*T*	8 cm	0.20 cm	0.20 cm	

[a]The experiment of setup A is upward propagating intrusion (rising); the experiments of setups B and C are thickening intrusions (opening) at a fixed depth with rectangular (*R*) or triangular (*T*) shape. Depth: depth of the top of the intrusion apparatus. Maximum thickness: in setup A, it corresponds to the cumulative thickness of the intrusions; in setups B and C, it corresponds to the maximum thickness of the intrusion apparatus top after the intrusion of 20 plates. Faulting thickness: thickness of the intrusion apparatus top when faults appear at the surface. The models described in this work are in bold.

To detect the vertical displacement of the model at the surface, we use a laser scanner with submillimeter resolution. The output of the scanner acquisitions is an *x*, *y*, and *z* matrix (where *x* and *y* are the map coordinates and *z* is the vertical component), representing the topography of the model at the moment of the scanning. We further compute and analyze the surface deformation at different times, subtracting successive deformation maps. The profiles along a section perpendicular to the intrusion obtained from the deformation maps in different time frames allow us to appreciate the vertical displacement during the experiment. In order to estimate the horizontal displacement (perpendicularly to the intrusion strike) at the surface, we acquire map images with a digital camera at different periods of intrusion (Figure 1). With the particle image velocimetry (PIV) technique, we extract the displacement field through image cross-correlation techniques [i.e., *Adam et al.*, 2005; *Ruch et al.*, 2012]. The displacement in successive digital images is first computed for small subsectors (interrogation window); here we use an interrogation window of 16×16 pixels, corresponding to 2×2 mm on the model. The merging of the subsector displacements allows appreciating the global displacement field. This technique is also applied in a few experiments on images acquired by a second camera from the side, detecting potential vertical and horizontal displacement fields in section view (Figure 1). Master optical and laser images are acquired before the experiments start, as reference for postprocessing deformation analysis. Slave image acquisitions are then systematically taken each 0.5 cm of vertical intrusion, in setup A experiments, and after each incremental metal plate insertion (0.5 mm) in setup B and C experiments. Finally, to fully exploit the 3-D evolution of faulting in the subsurface, we wet and cut the final models into slices of 0.5 cm, perpendicularly to the intrusion axis. This allows us to better analyze the deformation pattern at depth.

The time series profiles of vertical and horizontal deformations are performed by sampling a 2 cm wide swath data point across the deformation map and are further projected on a best fit line. This allows us to better identify the deformation signal and in particular to reduce the effect of any reflection of the laser on the sand grains. Where possible, these deformation profiles are extracted from the same swath of the most representative structural cross section.

The experiments are mostly devoted to simulate the long-term (~10^2 to ~10^4 years) deformation, as due to multiple intrusions. However, this is reached through an intermediate crucial step (insertion of 2–3 out of 20 plates), where the short-term experimental and natural deformations are also reasonably compared. This comparison allows calibrating and validating our results with simple and well-known cases of surface deformation triggered by single rifting episode (including Lakagigar, 1783, Iceland, or Dabbahu, 2005, Afar). This intermediate step allows a more robust longer-term comparison.

2.2. Scaling and Materials

Analogue modeling is the scaled reproduction of natural processes to understand the controlling key mechanisms. We impose a length ratio between model and nature ($L^* = L_{mod}/L_{nat}$) on the order of 10^{-4}–10^{-5} (1 cm in the model corresponds to hundreds of meters in nature). The density ratio between the model

and the nature is $\rho^* = \rho_{mod}/\rho_{nat}$. The mean density of the brittle upper crust in nature is 2700 kg/m^3. The mean density of the materials used to simulate the upper brittle crust in the analogue models is 1500 kg/m^3. Hence, $\rho^* = \rho_{mod}/\rho_{nat}$~0.6. The gravity ratio between the model and nature is $g^* = g_{mod}/g_{nat} = 1$. The product among ρ^*, g^*, and L^* has the dimension of a stress, allowing us to calculate the stress ratio between the model and nature: $\sigma^* = \rho^* g^* L^* = 0.6 \times 10^{-4}$–$0.6 \times 10^{-5}$. Then, we assume that natural rocks fail according to the Mohr-Coulomb failure criterion and have a mean cohesion of 10^7 Pa, with an angle of internal friction $\Phi = 35°$. Knowing the cohesion value in nature C_{nat} and the ratio between the cohesion in the model and in nature C^*, we calculate the cohesion of the material C_{mod} to use in the model; that is, $C_{mod} = C^* C_{nat} = 60$ to 600 Pa. The values of cohesion and internal friction are characteristics of the crushed silica sand (grain size = 40–200 μm), which we use to simulate the upper crust, similar to *Norini and Acocella* [2011] and *Ruch et al.* [2012].

Granular materials are often used in analogue models to simulate the main properties of the upper crust. Shearing tests on different granular materials demonstrate that they are characterized by an initial elastic behavior, followed by plastic behavior and then strain hardening prior the onset of brittle failure at the peak strength. The elastic strain stage is due to diffuse intergranular movements. Shear failure occurs when the grain displacement focuses along a localized zone [*Panien et al.*, 2006].

2.3. Assumptions and Limitations

Our dike analogues (metal plates) are inserted without external or remote stresses acting on the sand within the box, not simulating any regional tectonic contribution. As the aim of our work is to simulate the effect of discrete rifting episodes, each causing ~10 m of opening from a few days to a very few years [i.e., *Wright et al.*, 2006; *Ebinger et al.*, 2010], we neglect the much slower regional motion, in the order of centimeter per year or less.

In principle, the box hosting the sand may confine any deformation developed during the insertion of the plates. However, in all the experiments, the measured surface deformation diminishes away from the intrusion axis, reaching zero or anyway negligible values, within the noise range, toward the sandbox walls. This suggests that any boundary effect due to the confinement of the sand within the box may be neglected.

In setups B and C, we place a thin silicone layer between the glass of the box and the lateral termination of the intrusion apparatus, in order to avoid lateral sand dispersion. The silicone layer slightly reduces the opening of the sides of the intrusion apparatus next to the box walls. Even though this localized border effect may be considered a limitation of our experiments, in a few cases we tried to exploit its potential advantage. In fact, any peripheral cross section directly visible through the glass provides a snapshot of a deformation pattern less developed than that in the rest of the model, resembling a less advanced evolutionary stage. This apparently younger stage at the periphery of the intrusions may be compared to the more advanced stage visible in the cross sections throughout the rest of the model, adding complementary information on the evolution of the experiment. This complementary information is never used alone and has been always double-checked with independent data, as for example with experiments ending with younger stages of deformation in the central part of the model.

Another possible limitation concerns rare and minor asymmetries in the surface deformation developed in setups B and C. These may be related to the adopted sequence of manual insertion of the plates. However, any final asymmetry of the models is generally small, except from experiment B5, and is not significantly altering the results.

A potential limitation is represented by the difference in the spacing of the elements of the intrusion complex in model and nature. In nature, the dikes may focus in a narrow area but still showing host rock in between [*Walker*, 1958, 1960, 1963; *Gudmundsson*, 1983, 1995, and references therein; *Paquet et al.*, 2007], whereas in the experiments, the metal plates are all next to one another. This implies that the surface deformation in nature may resemble more complex and asymmetric patterns than in the experiments.

In our models we are simulating ideal isotropic conditions: any preexisting fracture, stiffness contrast, layering, and stress barrier that could significantly affect the intrusion-induced stress pattern, also enhancing stress concentration on specific layers [i.e., *Gudmundsson*, 2003; *Gudmundsson*, 2006, and references therein; *Philipp et al.*, 2013], is not included and is beyond the scope of the study. Finally, while many dikes responsible for rifting episodes in Iceland and Afar have propagated laterally [*Buck et al.*, 2006; *Ebinger et al.*, 2010;

Sigmundsson et al., 2014], our apparatus does not simulate any lateral propagation. In principle, this difference may partly affect our results: for example, laterally propagating shallow dikes may induce a narrower deformed area at the surface. However, these should be considered minor variations, and despite them, we expect that the overall surface deformation pattern due to dike emplacement is largely independent of the propagation direction of the dike.

3. Results

Eleven experiments have been performed (Table 1); here we present the results of the six most representative models only: one with setup A (upward moving metal plates; section 3.1), three with setup B (three models of gradually thickening intrusions with rectangular tip shape; section 3.2), and two with setup C (one model of gradually thickening intrusions with triangular tip shape; section 3.2).

3.1. Setup A: Upward Propagating Intrusions Experiment A2

In setup A models, we consistently find a marked uplift above the intruded plates, independently of their number (1 to 5 plates; Table 1). As the deformation pattern is best resolved with thicker intrusions, here we show model A2, in which 5 plates are intruded, with final thickness of 2.5 mm, propagating upward from the base of the table for 2.5 cm (Figure 2). Once the intrusions rise up to 1.5 cm, a 6 cm wide uplifted area (0.5 mm high) forms elongated above the intrusion, slightly asymmetric with respect to the intrusion axis. A continuous normal fault appears at the surface above the intrusion, slightly to the right (Figure 2b). Further moving the plates upward until the end of the experiment (2.5 cm of rise of the intrusion), the uplift above the intrusion increases up to ~1.5 mm (Figure 2c) and includes a discontinuous narrow apical graben (0.5 cm wide and $<$1 mm deep) bounded by normal faults (Figures 2c and 2d). In addition, 2–3 cm to the side of the graben, a continuous reverse fault striking parallel to the intrusion develops (Figure 2c). Section A-A′ (orthogonal to the strike of the intrusion), at the end of the experiment, reveals that the uplifted area is confined by two mostly blind inward dipping reverse faults (Figure 2d) departing close to the intrusion tip. They form a triangular wedge above the intrusion that moves upward (Figure 2l). At the wedge center, a shallow, not rooted, and discontinuous apical graben (~0.5 mm deep) is bordered by high-angle inward dipping normal faults with minor displacement with respect to the outer reverse fault. At times, the graben is replaced by a normal and reverse fault on one side of the intrusion (section B-B′ in Figure 2e). The horizontal displacement map at the end of the experiment (Figures 2h and 2i) shows that the surface moves ~0.4 cm away orthogonally to the intrusion axis. The PIV analysis on the side view of the experiment reveals that at depth this horizontal displacement focuses exactly above the intrusion; this displacement seems a consequence of the doming induced by the intrusion.

Very similar results, even though less pronounced, are obtained also for model A1, intruding only 1 plate.

3.2. Setups B and C: Thickening Intrusions at Constant Depth

We anticipate that the final deformation pattern strongly depends on the intrusion depth in setup B experiments (rectangular intrusive complex in section view) but not in setup C (triangular). For this reason, among the nine experiments, in this section we present three representative models of setup B and two of setup C (Table 1). For setup B, in order to appreciate the difference of the fault pattern with the depth to the top of the intrusive complex, we describe (1) experiment B1, having the shallowest intrusion depth (1 cm from the surface); (2) experiment B4, with medium intrusion depth (4 cm); and (3) experiment B6, with the largest intrusion depth (8 cm). For setup C, we describe (1) experiment C1, with a small intrusion depth (2 cm from the surface) and a sand cone above one side of the intrusions, and (2) experiment C2, with a medium intrusion depth (4 cm).

3.2.1. Experiment B1: Shallow Rectangular Intrusive Complex

The map view of the experiment shows that once 2 metal plates are intruded at 1 cm of depth, a depression forms above, at the surface (Figure 3b). Two parallel fractured areas 1.5 cm distant develop to the sides of the depression. These fractured areas consist of discontinuities formed by coalescing shorter fracture segments parallel to the intrusion axis. Our resolution does not allow us to define whether they formed as mode I (extension fractures) or mode II (normal faults) or both. Intruding additional plates (between 2 and 10), the fracture lengths increase and the fractures merge with neighboring ones. Once 10 plates (thickening of 5 mm) are intruded, these fracture zones become normal fault segments, dipping toward the center of the depression, or graben (Figure 3c). Meanwhile, minor fractures form within the graben. Inserting further plates, the graben

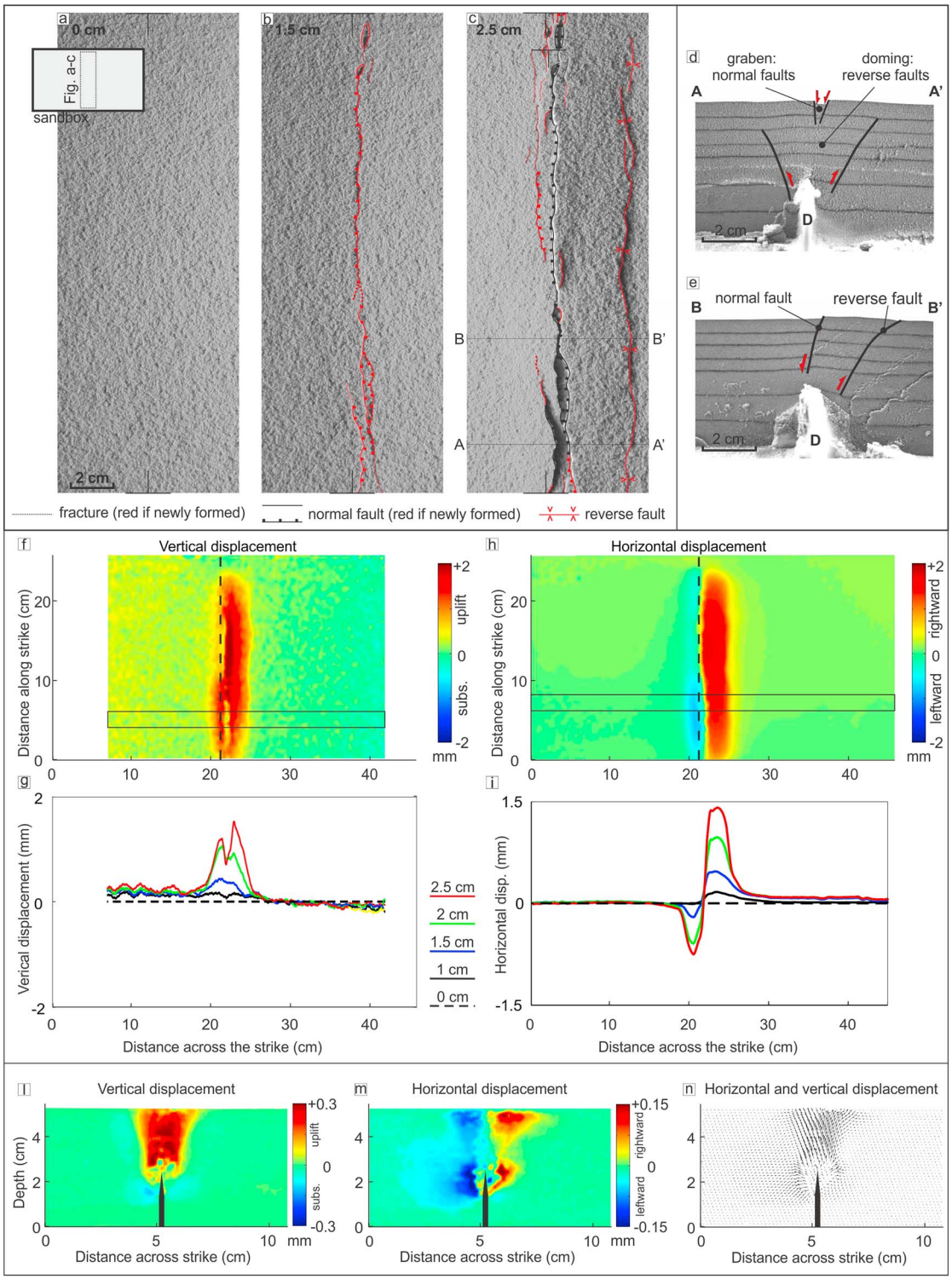

Figure 2. Summary of the results of experiment A2 (upward propagating dike; Table 1). Map views of the central part of the experiment (the dashed rectangle in the inset of Figure 2a shows the investigated area of the sandbox): (a) before the experiment starts, (b) after 1.5 cm, and (c) after 2.5 cm of rise of the metal plates. The plate position is indicated at the lower and upper edges of the maps. (d) Cross sections A-A′ and (e) B-B′; the main faults are marked by solid lines; the arrows indicate the sense of slip; *D* = dike complex (5 plates). (f) Vertical surface displacement map obtained with the laser-scanner at the end of the experiment and (g) vertical displacement profiles at different time frames of the experiment. (h) Horizontal surface displacement map at the end of the experiment and (i) horizontal displacement profiles at different time frames of the experiment. We only consider the horizontal displacement perpendicular to the dike strike, neglecting any component parallel to it. In both maps, the vertical dashed black lines show the position of the dike and the horizontal dashed gray lines the location of the time series profiles. (l) Vertical, (m) horizontal, and (n) total displacement field resulting from the PIV analysis of the side view images; the dike complex is indicated in black.

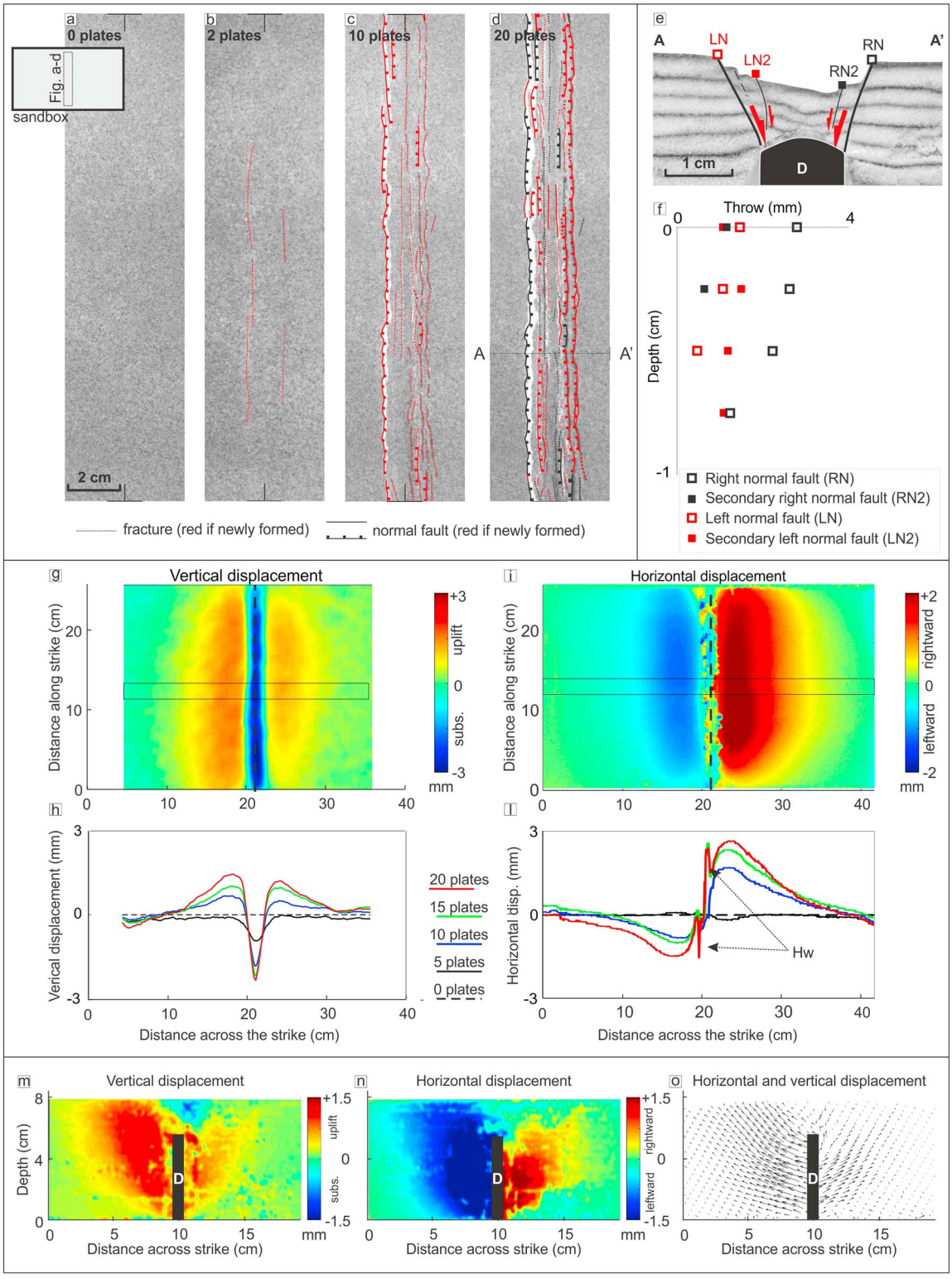

Figure 3. Summary of the results from experiment B1 (shallow thickening rectangular intrusive complex; Table 1). (a–d) Map views of the central part of the model for different steps of the experiment. The amount of intruded plates is reported in each image. (e) Cross section A-A′ in which the vertical throws of the faults are calculated at (f) different depths. *D* = dike complex (20 plates intruded). Each square on the graph shows the amount of vertical offset of the marker layer along the fault. Squares on the graph correspond to those of the section. (g) Vertical displacement map and (h) vertical displacement time series profiles; (i) horizontal displacement map and (l) horizontal displacement time series profiles. In the time series profiles the color of the profiles indicates the number of intruded plates. (m–o) Results of the PIV analysis from side view.

progressively enlarges and the distance between the border faults increases. The thickening of the intrusion complex increases the vertical throw and along strike length of the normal faults and the fractures. Therefore, the segments of normal faults and fractures merge along strike, forming two continuous conjugate border normal faults above the intrusion sides. These fault zones are well developed at the end of the experiment (20 intruded plates, for a total thickening of 1 cm at the intrusions tip; Figure 3d). At this final stage, secondary inner normal faults developed from the coalescence of the fractures within the graben (Figure 3d).

The cross section A-A′ at the end of the experiment shows that the depression is bordered by two main inward dipping normal faults (conjugate faults), forming a graben-like structure rooted to both sides of the intrusion's top, with minor normal faulting within (Figure 3e). In order to better characterize the kinematics of the faults, their vertical throw has been measured at various depths in the section. Both the border and secondary faults have the highest vertical offset at the surface (2–3 mm), decreasing linearly with depth (Figure 3f).

The vertical deformation map and related time series profiles show that the incremental thickening of the intrusions induces two uplifted areas to the sides of the intrusions and the subsidence of the sand above the intrusions, delimiting a 6 cm wide depression. At the end of the experiment, the subsidence reaches ~2.5 mm and the uplift ~1.5 mm (Figures 3g and 3h). The horizontal displacement map and profiles show that the widening of the intrusion at depth causes a progressive divergent displacement of the surface (up to ~2.8 mm) with respect to the intrusion axis (Figures 3i and 3l).

To better capture the cumulative displacement field, we use the section view PIV analysis during the experiment (Figures 3m–3o), plotting the vertical and horizontal components of the displacement. The horizontal component, highest close to intrusions and decreasing upward, shows a diverging motion of the sand to the sides of the intrusion (Figure 3n). However, in the wedge directly above the intrusions the horizontal deformation is negligible (Figures 3n and 3i), consistently with the fact that the maximum horizontal deformation at the surface is ~5 cm aside from the intrusions axis (Figure 3l). The vertical component of displacement (Figure 3m) shows that the host rock to the sides of intrusions moves upward, whereas the wedge above the intrusions subsides (Figures 3m and 3o), similar to what is observed at the surface (Figure 3g). These motions result from the lateral push of the sand by the intrusions thickening at depth, enhancing outward and, in turn, upward displacements of the sand to the intrusion sides and extension and thinning the wedge above the intrusions (Figure 3o).

Experiment B2 (2 cm deep intrusive complex) shows an overall deformation pattern (i.e., graben width, inward dipping border normal faults, and minor normal faults within the graben), magnitude of the deformation (i.e., amount of subsidence, and uplift, fault displacement), and fault kinematics very similar to those of experiment B1; therefore, B2 is not shown here.

3.2.2. Experiment B4: Medium Depth Rectangular Intrusive Complex

The map view of the experiment after the insertion of 3 plates at 4 cm of depth shows a 1 cm wide depression at the surface above the intrusions (Figure 4b). With the insertion of 4 plates, two continuous and parallel faults develop symmetrically to the sides of the depression (Figure 4b). After the insertion of 6 plates, two distributed outer fracture zones begin to form at a distance of 0.7 cm from the previous fault zones (Figure 4c). After 6 plates, the deformation at the surface is mostly accommodated by the outer fracture zones, while the inner faults do not develop further. As in B1, the fracture zones are first formed by minor segmented structures, progressively increasing their vertical throw and merging along strike to form a single continuous border fault at each intrusion side (Figure 4d). Once the border faults are formed, they are repeatedly activated at each injection, increasing their throw. On both sides of the intrusive complex, the surface of the model between each pair of internal and outer faults is tilted inward up to 20–30° (Figures 4d and 4l). The vertical displacement profiles show that during the first stages of the experiment (5 plates), a 0.6 mm deep depression forms above the intrusions and a 0.1–0.2 mm uplift develops to its sides (Figure 4f). This early stage corresponds to the formation of the inner set of faults. The subsidence within the depression increases when 10 plates are inserted and the outer fracture zones develop. At this time, the outer uplift becomes asymmetric and increases up to 0.3 mm only at one side of the intrusions. Intruding more than 10 plates, the subsidence reaches the highest value (~3.5 mm) above the intrusions (Figures 4e and 4f). The maximum uplift reaches 0.6 mm on one side of the intrusions, delimiting a final central 6 cm wide depression. Despite the uplift asymmetry, the overall vertical displacements profiles are similar to B1. The horizontal displacement map and the time

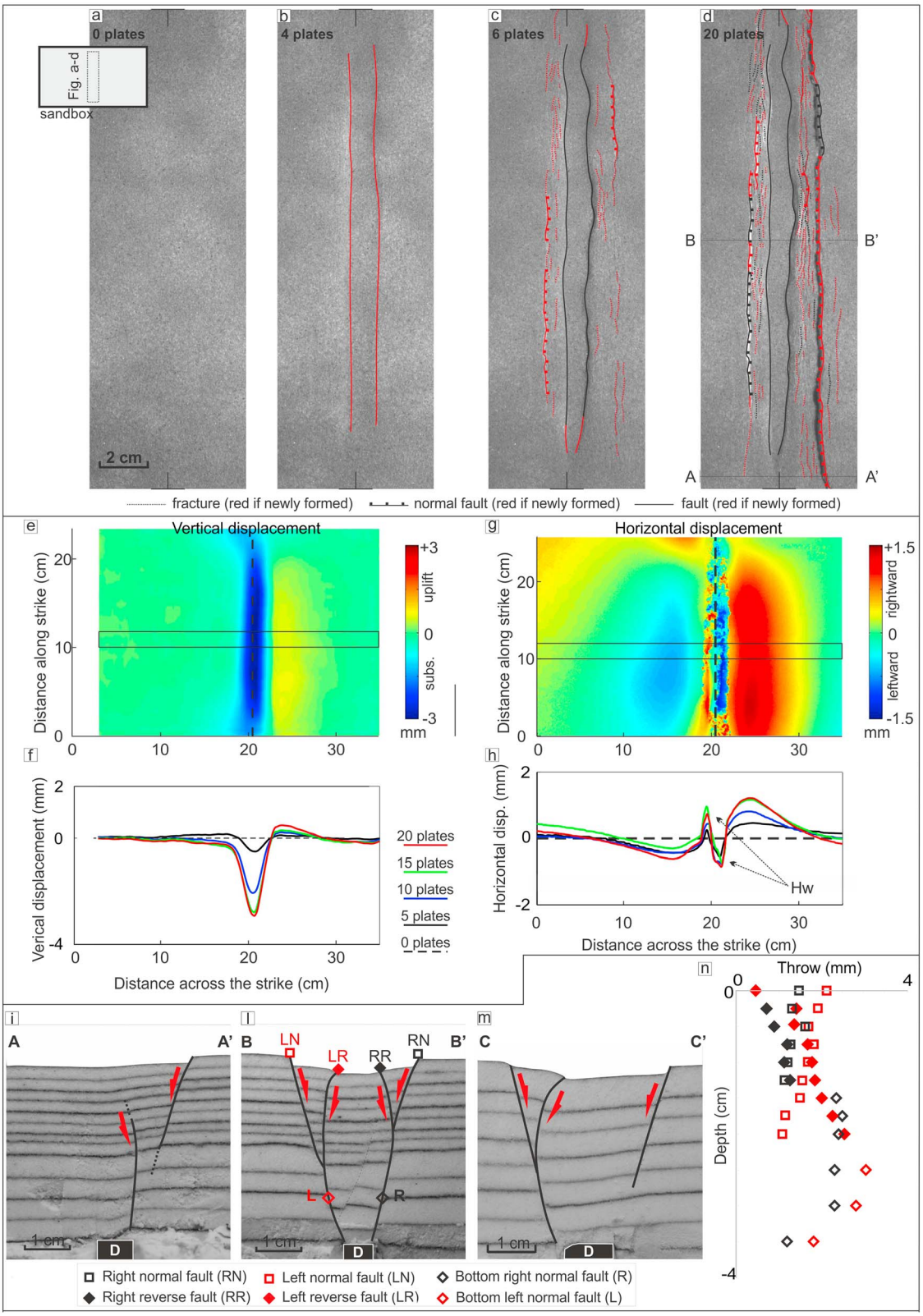

Figure 4. Summary of the results for experiment B4 (medium depth opening rectangular intrusions; Table 1). (a–d) Map views of the central part of the model for different evolutionary stages. (e) Vertical displacement map and (f) vertical displacement time series profiles; (g) horizontal displacement map and (h) horizontal displacement time series profiles; (i) cross sections A-A′ and (l) B-B′; (m) cross section C-C′ from the central portion of experiment B5. *D* = dike complex (20 plates intruded). (n) Variation in the vertical displacement of the faults in section B-B′; symbols on the graph correspond to those of Figure 4l.

series profiles (Figures 4g and 4h) show an overall divergent, extensional motion. However, within the depression there is also an inward horizontal motion, as indicated by the two symmetric peaks on the profiles close to the central axis, in correspondence with the tilted blocks enclosed between the outer and inner faults (Figure 4h).

At the end of the experiment, in order to capture also an intermediate stage of evolution, we consider peripheral cross section A-A′ (Figures 4d and 4i). Here as anticipated in section 2.3, the deformation is smaller than that in the rest of the model; the faults form only on one side of the intrusions and are not completely developed. The inner high-angle fault is better defined at depth, close to the intrusions tip, and disappears upward, where the marker layers are bent but not faulted (Figure 4i). This fault dips inward at its base and then outward at its top, showing an arcuate shape in section view. Thus, the fault is normal below the maximum curvature and reverse above. The outer inward dipping fault is normal and well defined at the surface but gradually disappears with depth. This section shows that inner arcuate fault and the outer normal fault are two distinct structures.

Section B-B′, along the center of the model (Figures 4d and 4l), reveals the final stage of deformation. Here the two parallel and continuous inner fault zones observed at the surface correspond to two high-angle arcuate faults, normal at their base and reverse at their top. The outer normal faults are inward dipping and connect to the reverse faults at their maximum curvature points.

Figure 4n shows the variation of the vertical throw of both the normal and arcuate faults in the central section B-B′. To better understand the kinematics of the faults, we separate the throws measured above and below their junction. We separately display the throws of the inner arcuate faults (LR and RR) and those of the outer normal faults (LN and RN) above the junction from those measured on the left and right arcuate faults below the junction (L and R) (Figures 4l and 4n). Above the junction, the vertical throw of the inner reverse faults (LR and RR) increases downward. Conversely, the vertical throw of the outer normal faults (LN and LR) decreases downward. This confirms that at each side of the intrusive complex above the junction, the deformation is partitioned on two faults, while below the junction it is accommodated by a single fault with greater slip.

The intrusion of the 4 cm deep rectangular complex has been simulated twice (experiments B4 and B5). Experiment B5 shows an asymmetry of the graben structure (Figure 4m), also coinciding with a minor temporary asymmetry in the configuration of the intrusive complex. In the cross section of B5 (section C-C′ in Figure 4m), the left side of the graben shows the same structure as B4: a branched fault resulting from the combination of an inner arcuate fault (reverse at the surface) and an inward dipping outer normal fault. The opposite side of the graben is marked by an inward dipping normal fault that vanishes downward (Figure 4m). A 3 cm deep rectangular intrusion (B3) has been also tested, with an overall deformation pattern mostly similar to B4.

3.2.3. Experiment B6: Deep Rectangular Intrusive Complex

After the insertion of 10–12 plates at a depth of 8 cm, a depression forms at the surface above the intrusions; this is better defined (0.3 mm of depth) when bordered by two continuous faults, 1.5 cm distant (Figure 5b). After the insertion of 14 plates, an outer fracture zone develops to the outer side of the faults, at a distance of 1.5 cm (Figure 5c); normal faults coalesce along this fracture zone. Increasing the intrusions thickness up to 1 cm (20 plates inserted; Figure 5d), the inner and outer faults at the sides of the intrusions become better defined, even though still discontinuous. The outer fracture zones broaden the depression, which becomes 5.5 cm wide and 2.2 mm deep (considering both the uplifted and the subsided parts). However, here the outer faults are more distant and less defined than in B4 experiment. The maximum absolute subsidence is 1.8 mm above the intrusions, and the uplift is <1 mm to the intrusion sides (Figures 5e and 5f). The horizontal surface deformation map displays a low signal/noise ratio and is not shown.

At the end of the experiment, to capture also an intermediate state of evolution of the model, we consider peripheral cross section A-A′: this shows a depression with two blind inner arcuate faults, without any fault at the surface (Figure 5g), as observed in B4. Conversely, in cross section B-B′, at the center of the model, the arcuate faults reach the surface (Figure 5h). The outer normal faults are here absent, appearing only in other cross sections, and the depression is bordered by the two inner arcuate faults propagating from the intrusion top. The fault throw of the arcuate faults increases from the surface to 4 cm of depth (area of maximum curvature); below the throw becomes constant or slightly decreases (Figure 5i).

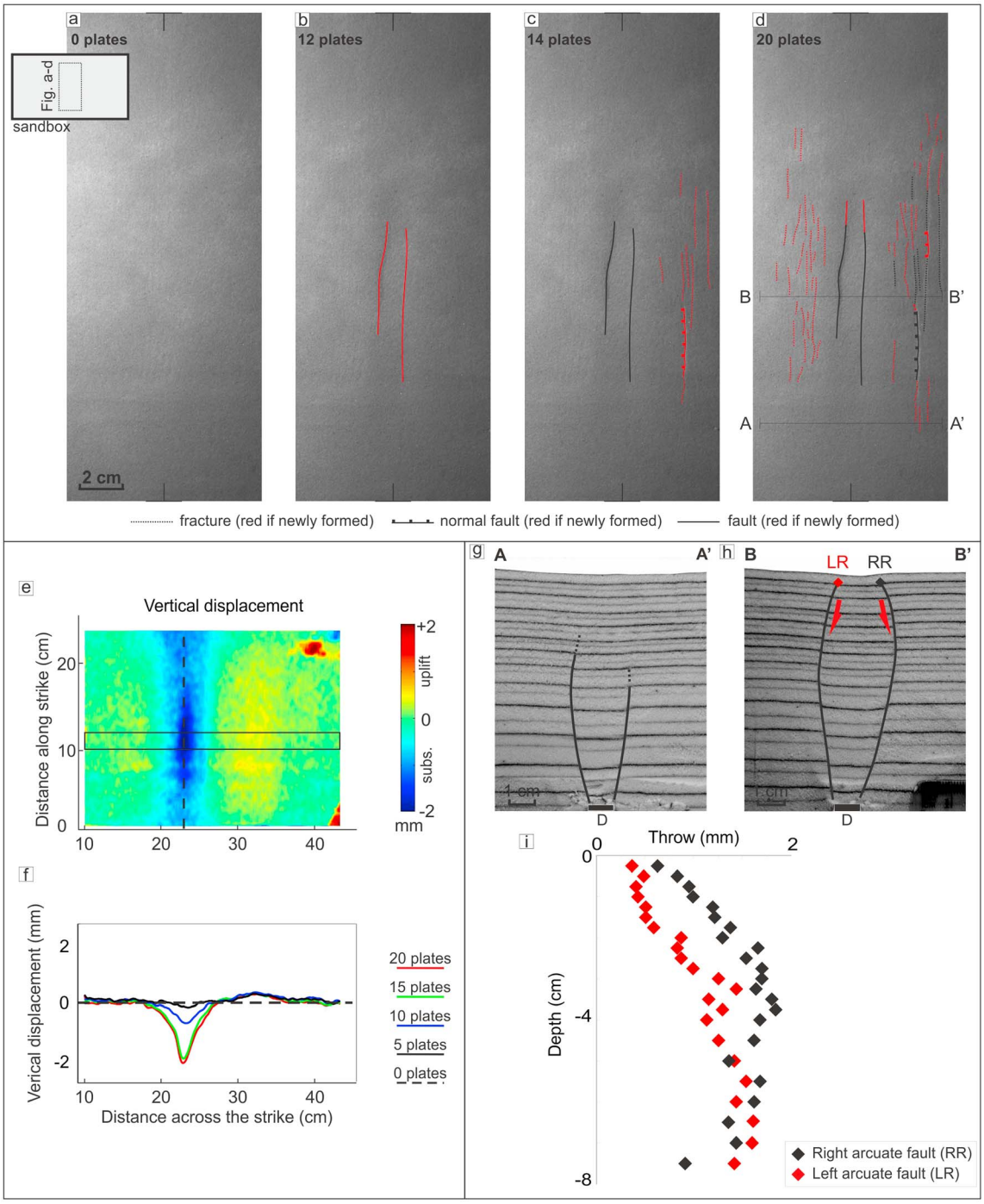

Figure 5. Results for experiment B6 (deep thickening rectangular intrusion; Table 1). (a–d) Map views of the central part of the model for different stages. (e) Vertical displacement map and (f) vertical displacement time series profiles. (g) Cross section A-A' and (h) B-B'; *D* = dike complex (20 plates intruded). (i) **V**ertical throws pattern of the faults in section B-B'.

3.2.4. Experiment C1: Shallow Triangular Intrusive Complex

In this experiment, the intrusive complex has a triangular shape in section view and is placed at 2 cm of depth, so that it can be compared to experiment B2. In addition, in order to test also the role of the topography, we have placed a 3 cm high and 9 cm wide sand cone above the intrusions, toward one side of the box (Figure 6a): indeed, preexisting monogenic or polygenic volcanic cones are often found along rift zones, possibly affecting the deformation pattern induced by diking. Intruding one plate, in the flat area

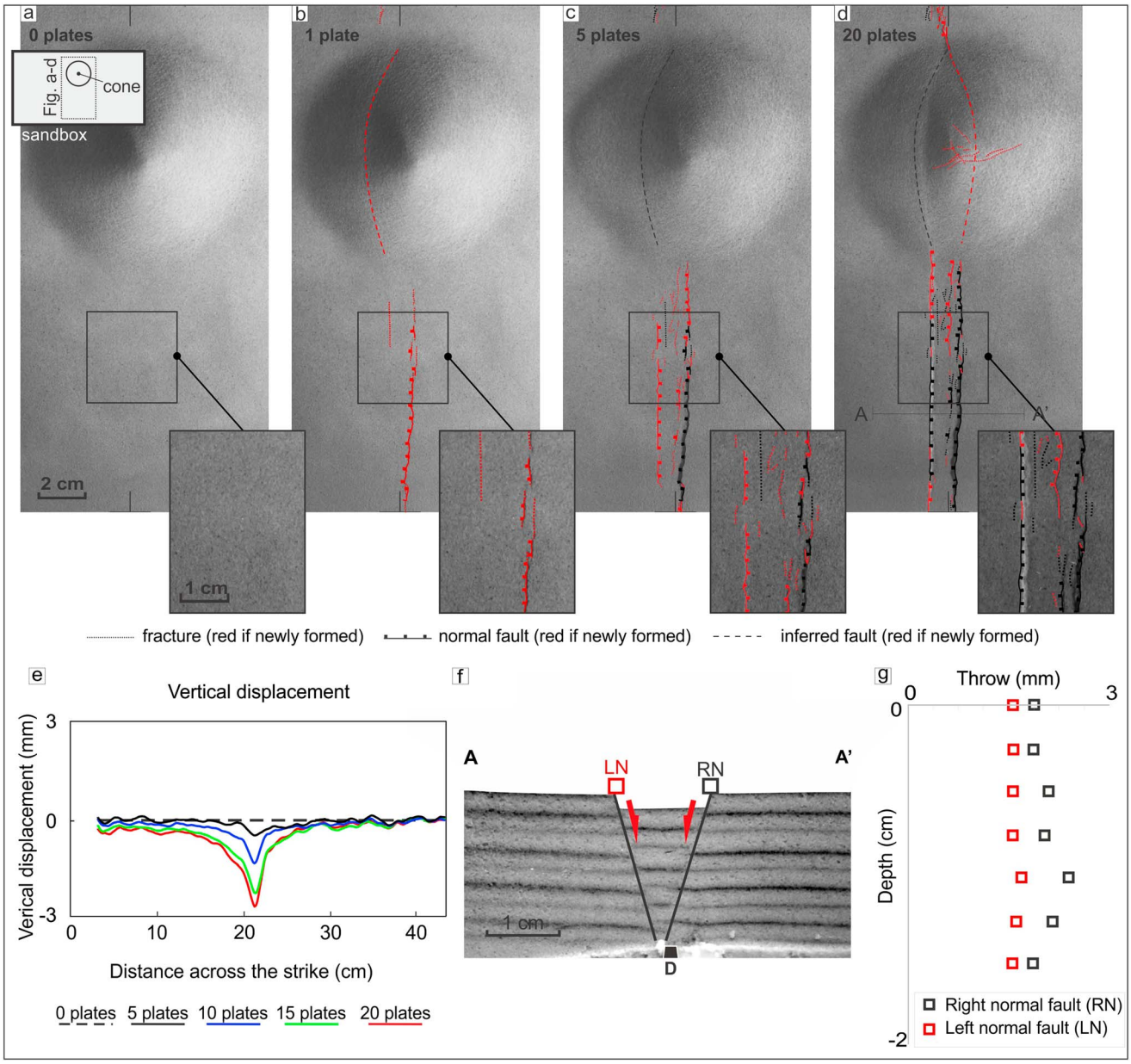

Figure 6. Results of experiment C1 (shallow triangular intrusive complex with a cone above; Table 1). (a–d) Map views of the central part of the model at different stages. (e) Vertical displacement time series profiles across the graben in the central portion of the experiment. (f) Cross section A-A'. *D* = dike complex (20 plates intruded). (g) vertical throws pattern of the faults in section A-A'.

away from the cone, a continuous normal fault appears at the surface ~0.5 cm to one side of the intrusion axis; the fault terminates in a series of fractures vanishing toward the cone. To the other side, a short fracture forms on the flat area and a normal fault on the cone (Figure 6b). Intruding more plates (2 to 5 plates) shorter fault segments develop on both sides of the intrusions. These define an ~1.2 cm wide and 0.5 cm deep depression (Figures 6c and 6e); minor fractures form within. On the cone, the previously formed fault grows (Figure 6c). Intruding more than 5 plates, in the flat area, the border fault segments merge along strike, deepening the depression (Figure 6e). At the end of the experiment (20 plates intruded), in the flat area, the depression is defined by one continuous fault on one side and two fault segments on the other. Secondary normal faults locally develop from the fractures within the depression. At this final stage, the faults are well developed also on the cone, where they are more distant (~2.5 cm) than in the flat area (~1.2 cm) (Figure 6d).

The vertical displacement time series profiles across the graben highlight that the final subsidence of the depression reaches 2.1 mm, with negligible uplift to the sides (Figure 6e). Cross section A-A′ reveals that the depression is a graben formed by two inward dipping normal faults, geometrically connected to the intrusion top (Figure 6f). The throw of the faults is almost constant with depth (Figure 6g).

3.2.5. Experiment C2: Medium Depth Triangular Intrusive Complex

The map view of the experiment shows that after the insertion of 2 plates at 4 cm of depth, a fracture zone forms 2 cm to one side of the intrusions (Figure 7b). With 8 inserted plates, a continuous fault forms from the coalescence of these fractures. On the opposite side, fractures and smaller normal faults start to develop (Figure 7c), delimiting a $<$1 mm deep depression above the intrusions (Figure 7f). Inserting more than 8 plates, the faults and fractures on both sides grow and the depression further subsides (Figure 7f). At the end of the experiment (20 plates; Figure 7d) the main fault on the one side is partly flanked by an inner secondary continuous fault at a distance of 0.8 cm, whereas on the other side the main fault is flanked by outer shorter faults and fractures at a distance of 0.8 cm (Figure 7d). The subsidence of ~1 mm above the intrusion, without any uplift to the sides, delimits a 5.5 cm wide depression. The subsidence is less than half of that observed in B4, having the same intrusion depth but different final intrusion shape (Figures 4f and 7f).

Section A-A′ in the peripheral part of the depression, against the Plexiglas wall, shows that the faults are normal and inward dipping, disappearing downward (Figure 7g). Central section B-B′ confirms that the depression is bordered by two inward dipping normal faults decreasing their vertical throw with depth (Figures 7h and 7i). The vertical throw is here 0.5–1 mm smaller than that of the normal faults in B4 (Figures 4m and 7i).

The overall geometry of the graben in C2 is similar to that of C1 (2 cm deep triangular intrusions) and C3 (8 cm deep triangular intrusions) experiments. The main difference among the three models with setup C regards the amount of surface deformation, that is progressively smaller (1–2 mm) but wider (up to 5.5 cm) increasing with the intrusion depth. In fact, despite the overall similar graben structure, the normal faults in C3 do not fully reach the surface.

4. Discussion

4.1. Overall Deformation Pattern and Setup Relevance

A first significant difference in the deformation pattern has been observed between the upward propagating intrusions (setup A) and the intrusion thickening at constant depth (setups B and C). In setup A, the intrusions push the overburden up (Figure 2l), resulting in a doming delimited by major reverse faults with shallow and secondary apical graben (Figures 2c, 2d, 2f, and 2g). Surface uplift bounded by reverse faults has been previously obtained in analogue models simulating dike emplacement, by injecting vegetable oil in sand [i.e., *Abdelmalak et al.*, 2012] or viscous intrusions with silicone in sand [*Acocella et al.*, 2001]. However, analytical, geological, and geodetic data [i.e., *Rubin and Pollard*, 1988; *Bonaccorso*, 2003; *Buck et al.*, 2006; *Dzurisin*, 2006; *Wright et al.*, 2006; *Rowland et al.*, 2007] show that dike emplacement mainly produces a depression within a broadly uplifted area, not confined by any reverse fault. This deformation pattern is different from that observed in setup A, where most of the deformation focuses on the uplifted area bordered by reverse faults. Therefore, the deformation pattern of setup A is considered as poorly realistic for dike emplacement.

In setups B and C, a main depression, delimited by normal faults, typically forms at the surface above the intrusions; the depression is bordered by slightly uplifted areas not confined by any reverse fault (Figures 3–7). The overall deformation pattern of these experiments is comparable to that obtained by *Mastin and Pollard* [1988], where normal faults form a graben above the intrusions, with minor younger faults within, also showing an increase of the graben width with the intrusion depth (Figure 11a). In addition, a thrust fault within the graben has been also highlighted by *Mastin and Pollard* [1988]; this feature, even though minor and poorly represented, may be reconciled with the arcuate inner faults of our models. Despite these general similarities, it is noteworthy that in *Mastin and Pollard* [1988], unlike our experiments, there was not any substantial variation of the graben structure and fault kinematics with different intrusion depths and shapes. This may be partly related to the different granular material, which was more cohesive in *Mastin and Pollard* [1988] and induced more extension fractures at the surface, with minor or less evident faulting.

The image processing results (laser scanner and PIV) provide detailed vertical and horizontal displacement maps and profiles, showing subsidence above the intrusions and uplift to the sides, with a maximum

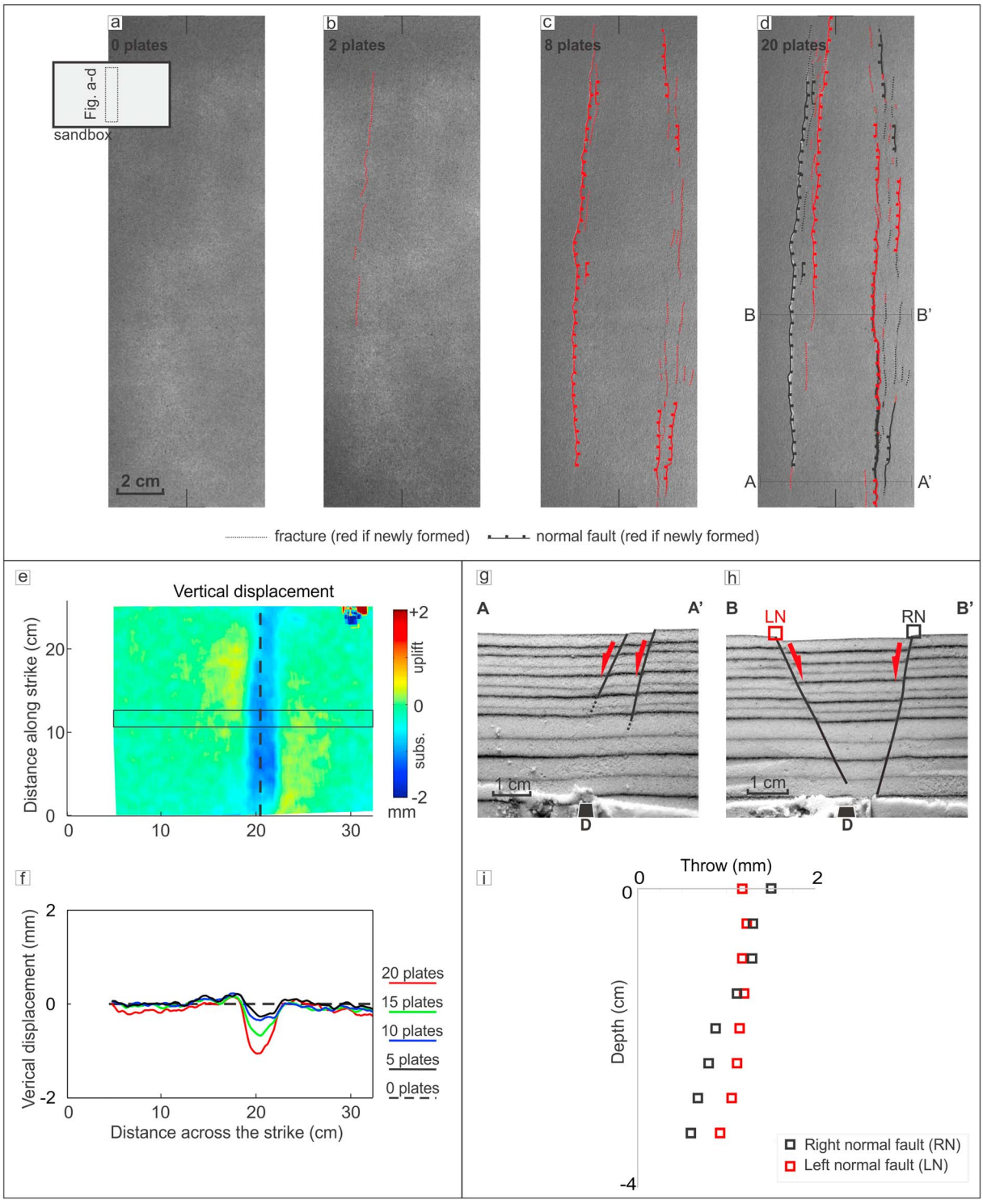

Figure 7. Results of experiment C2 (medium depth triangular intrusive complex; Table 1). (a–d) Map views of the central part of the model at different stages. (e) Vertical displacement map and (f) vertical displacement time series profiles. (g) Cross sections A-A′ and (h) B-B′. *D* = dike complex (20 plates intruded). (i) Vertical throws pattern of the faults in section B-B′.

horizontal displacement to the side of the intrusions and a minimum above it (i.e., Figure 3l). The overall vertical and horizontal deformation pattern of our experiments is also consistent with that of numerical and analytical models [i.e., *Dieterich and Decker*, 1975; *Rubin*, 1992; *Dzurisin*, 2006, and references therein]. In addition, our results are consistent with those obtained by geologic and geodetic data during dike-induced rifting events or

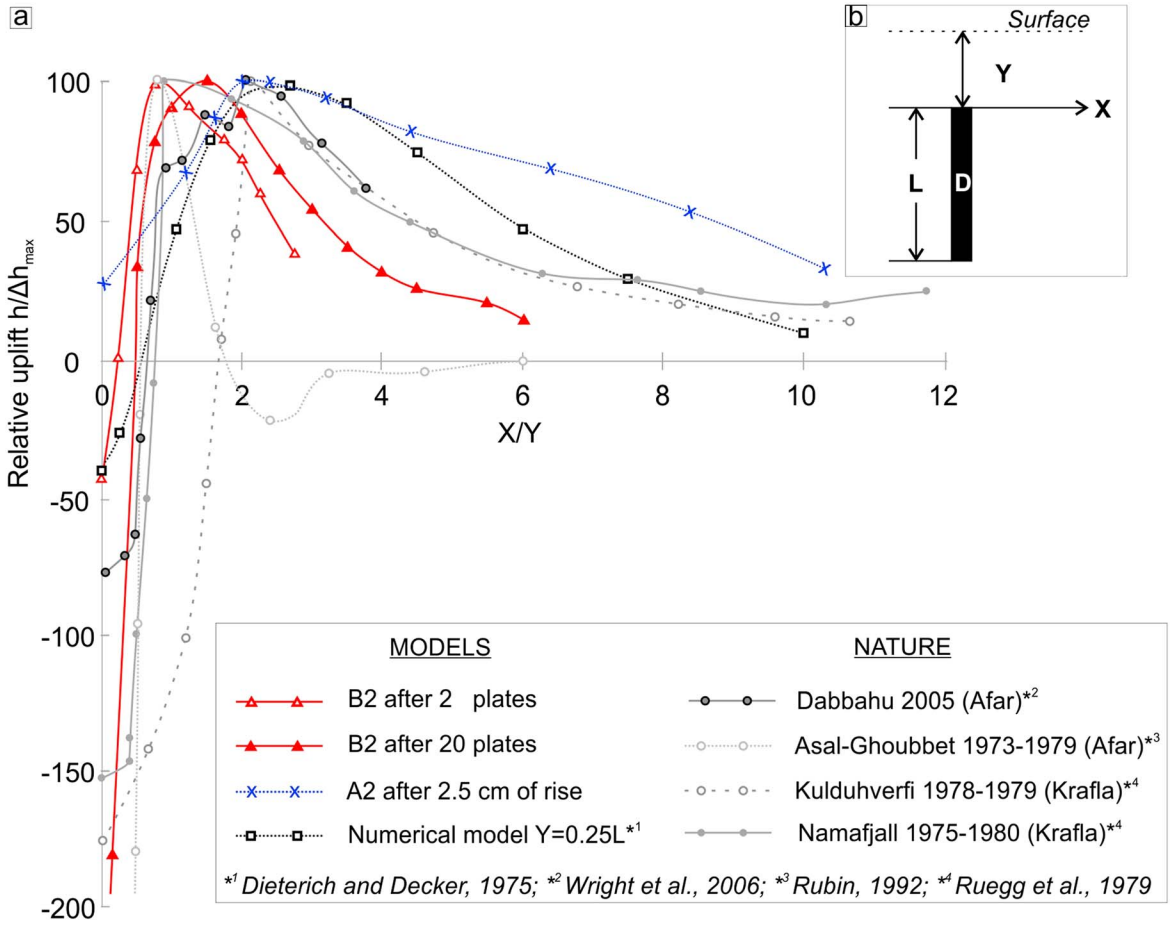

Figure 8. (a and b) Surface vertical displacement, expressed as a function of the amount of uplift h relative to the maximum uplift Δh_{max} versus the lateral distance from the intrusion axis *X* with regard to the top of the intrusion *Y*, for a numerical model (in which the depth of the dike top is 0.25 times the dike length) [*Dieterich and Decker*, 1975], our A2 and B2 experiments and four rifting events in Afar and Iceland (see text for details). In Figure 8b: *L* is the dike height, *Y* is the depth of the dike top, and *X* is the horizontal distance from the dike complex (*D*) [*Dieterich and Decker*, 1975].

episodes [i.e., *Pollard et al.*, 1983; *Rubin and Pollard*, 1988; *Jónsson et al.*, 1999; *Cervelli et al.*, 2002; *Wright et al.*, 2006; *Rowland et al.*, 2007; *Keir et al.*, 2009; *Pallister et al.*, 2010; *Nobile et al.*, 2012; *Sigmundsson et al.*, 2014]. For example, the overall patterns of the horizontal and vertical displacement maps and profiles of experiment B1 (Figures 3g–3i and 3l) are similar to those of the Dabbahu rifting event (2005, Afar) [*Wright et al.*, 2006] and the Krafla rifting episode (1975–1984, Iceland) [*Rubin*, 1992]. For a more quantitative approach, we compare the measured vertical surface deformation of models A2 and B2 with that from numerical models [*Dieterich and Decker*, 1975] and natural examples of rifting episodes. The latter include the episodes and events in Afar (Asal-Ghoubbet in 1978 and Dabbahu in 2005) [*Ruegg et al.*, 1979; *Wright et al.*, 2006] and Iceland (at Kulduhverfi in 1978–1979 and at Namafjall in 1975–1980, both in the Krafla magmatic system) [*Rubin*, 1992]. The vertical displacements are normalized to the total vertical displacement as a function of the distance from the intrusion *x* normalized to the intrusion depth *y* (Figure 8). The numerical model describes the elastic behavior of the host rock under dike injection, without any faulting. The natural examples show both the elastic and anelastic behavior of the crust during diking, where extension fractures and normal faults are also generated. In order to better compare these behaviors with our data, we consider the vertical displacement in model B2 after the insertion of 2 plates, when the faults are not yet formed (i.e., elastic behavior, see section 2.2), and after the intrusion of 20 plates, when the faults are well developed (anelastic behavior); these are meant to detect the deformation in the early and late stages of intrusions, respectively. The deformation curve of our experiment shares an overall similar pattern to that of the numerical model, with minor negative values (indicating absolute subsidence) close to the intrusion axis and positive values (absolute uplift) reaching a maximum followed by decay

away from the intrusions. However, the maximum deformation in the experiments is closer to the intrusion axis than in the numerical model, showing a more marked deformation curve. This suggests that the sand in the experiments carries only a portion of the elastic behavior of the numerical model, due to the diffuse intergranular slip in the sand particles before developing any shear zone [i.e., *Panien et al.*, 2006]. The anelastic curve of B2 after the intrusion of 20 plates shows much higher negative displacements close to the intrusion axis, indicating greater subsidence above the intrusion than in the numerical model. The subsidence above the intrusions in B2 results from the thickening of the intrusions, which extends the sand above, as suggested by the side PIV images (Figure 3m). The deformation curves obtained measuring the deformation during diking events or episodes in nature show a common remarkable subsidence ($>$70% of Δh_{max}) above the intrusion, even though their magnitude and width may vary. Therefore, despite any difference in amplitude, the experimental displacement curves are comparable to those of the natural cases with surface faulting and developing a graben above the intrusions. Such a faulting explains the discrepancy between the elastic numerical models, where the subsidence appears negligible, and the natural cases, where the subsidence is larger and bounded by faults. The amount of subsidence in model B2 after the intrusion of 20 plates is significantly greater than that shown by the natural cases, suggesting a more advanced stage of dike-induced rifting, where multiple dikes are intruded reactivating graben faults.

The displacement curve of experiment A2 does not show any negative value close to the intrusions axis, conversely to B2, the numerical model and nature. This confirms that setup A is poorly representative to study the deformation induced by dikes. Overall, the comparison among the displacement curves suggests that the surface deformation observed in setups B and C is a good approximation of nature. This indicates that despite the general limited elasticity of sand, the intergranular sliding of the sand grains in our experiments may satisfactorily approximate the overall elastic behavior of the natural rocks for low stresses. Moreover, the use of sand allows us to enter also the anelastic domain, where the conditions for the stress concentration are met.

More in general, the different results obtained in our three experimental setups, as well as this preliminary comparison to natural data, suggest a model for dike propagation essentially governed by the horizontal opening of the dike walls (as in the setups B and C), without upward push (or mass translation in the direction of propagation) of the intrusions (as in the setup A). This implies that the end member process described in experimental setup A has a negligible importance during diking in nature. This also suggests a general model of dike propagation where the indefinite repetition of two stages captures the essential steps of a continuum process: (a) the dike first focuses the stresses at its tip, inducing a gas-filled mode I fracture of negligible thickness with regard to that of the dike (Figure 9a), and (b) the magma progressively penetrates the fracture, enlarging it and pushing the two walls aside, until the intruded fracture reaches the same thickness as that of the main body of the dike (Figure 9b). The continuous repetition of these two stages allows the propagation of the dike only through the lateral expansion of its sides, without any upward push. This model may be applied also to laterally propagating dikes. Therefore, the surface deformation observed during dike emplacement appears much more related to the thickening of the intrusion, rather than the translation of the host rock in the direction of propagation. Furthermore, any increase in the dike length may further thicken the dike, which may vary its overall thickness during a longer-distance propagation, even if not shown in Figure 9.

The model obtained comparing setups A and B and summarized in Figure 9 provides an experimental confirm of previous theoretical predictions, in which the dike is considered a mode I opening fluid-filled fracture where the horizontal displacement induced by the opening dike walls is much larger than the dike-parallel displacement [i.e., *Westergaard*, 1939; *Pollard*, 1987].

4.2. Effect of the Intrusion Depth and Geometry on the Deformation

In setup B the deformation pattern varies with the intrusion depth (Figure 10a). The graben of the model with shallowest intrusions (1 cm in B1) is bordered by normal faults. For 4 cm deep intrusions, the depression is bordered by inner arcuate faults and outer inward dipping normal faults (B4). The deepest intrusions, at 8 cm, form almost exclusively arcuate faults (B6). Despite the similar final vertical deformation pattern at the surface (a central depression and uplifted areas to the sides), increasing the intrusion depth decreases the subsidence and uplift at the surface (Figures 10a and 11b), resulting in a progressively shallower depression

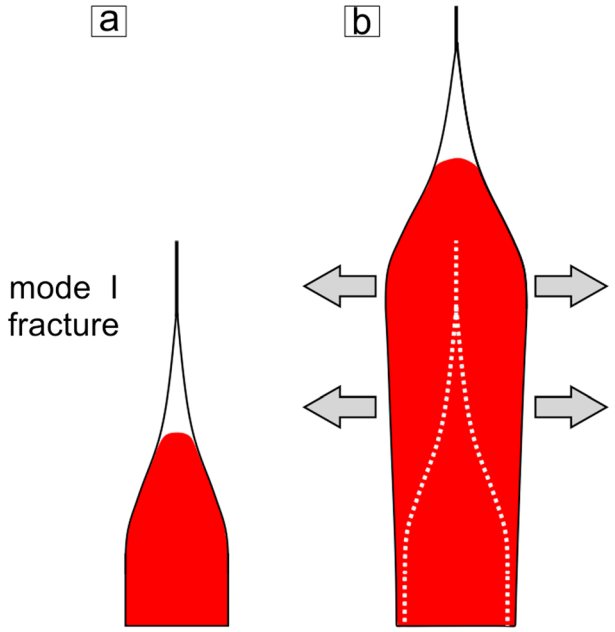

Figure 9. Model of dike propagation in two stages, which repeat indefinitely in a continuum process: (a) the dike focuses the stresses at its tip, inducing a mode I fracture; (b) the magma progressively penetrates the fracture, enlarging it and pushing the two walls aside.

(Figure 11c). Moreover, the deepest the intrusions, the highest the distance at the surface between the peripheral normal faults, forming wider depressions (Figures 10a and 11a).

In setup C the deformation does not vary with the injection depth (Figure 10b). The graben is always bordered by two conjugate normal faults, whose distance at the surface increases with the intrusion depth (Figure 11a). The final vertical displacement profiles also show a central subsidence and minor lateral uplift, whose extent decreases with the intrusion depth (Figures 10b and 11b). However, differently from setup B, in setup C the subsidence in the 4 cm deep experiment is ~30–50% lower and in all the experiments the uplift is negligible (Figure 11b). This is also in accordance with the fact that for an equal depth of intrusion, the fault throws measured in setup B are 1–2 mm larger than in setup C (Figures 4m and 7i). All these differences suggest that the subsidence, and especially the uplift at the surface, depend on the intrusion depth and overall configuration.

In order to better understand the effect of the thickening of the intrusions on the sand, we focus on the cross correlation imagery from the side view of model B1 (PIV analysis; Figures 3m–3o). This shows how the thickening of the intrusive complex promotes subsidence above and uplift to the sides by means of lateral compression of the material. The lateral compression (or lateral displacement) of the sand and the related subsidence and uplift at the surface are proportional to the intrusion thickening. Since the overall thickening at the intrusive complex tip is higher in setup B than setup C, we expect higher surface deformation in setup B. Hence, we suggest that the lack of uplift and the shallower depression in setup C (Figures 10 and 11c) is caused by the lower final opening of the upper tip of the intrusion apparatus in setup C (0.2 cm) than in B (1 cm). This indicates that the final shape of the dike complex in section view (rectangular or triangular) may affect the deformation at the surface and shape the topography. In addition, the increase in the intrusion depth increases the lithostatic pressure above, which in turn limits the uplift of the surface to the sides of the intrusions. Therefore, the higher the intrusion depth, the lower the uplift to the sides (Figures 10 and 11). These considerations suggest that the overall deformation pattern is controlled by the interplay between the intrusion depth and its thickness, consistently with previous studies [*Pollard and Holzhausen*, 1979; *Pollard et al.*, 1983; *Mastin and Pollard*, 1988; *Rubin and Pollard*, 1988].

4.3. Fault Propagation

Two types of faults form in our experiments, differing in geometry and kinematics: normal faults and arcuate normal/reverse faults (Figure 12). The study of the cross sections and fault throws allows us to better define their kinematics and development.

4.3.1. Normal Faulting

At the surface, at the side of the dike the maximum compressive stress ($\sigma 1$) is subvertical [*Rubin and Pollard*, 1988; *Patton and Fletcher*, 1995; *Bonafede and Danesi*, 1997; *Gudmundsson and Loetveit*, 2005]. This enhances the formation of vertical extension fractures and the high-angle normal faults observed in the experiments. However, one debated aspect regarding faulting induced by diking is whether the faults nucleate at the surface or at depth. In our models, the throw of the normal faults in the central portions of the models is usually highest at the surface, decreasing downward (Figures 3f, 4m, 7i). In the peripheral cross sections, where the deformation is smaller, the normal faults are still well defined at the surface and gradually disappear at depth (Figures 4i and 7g).

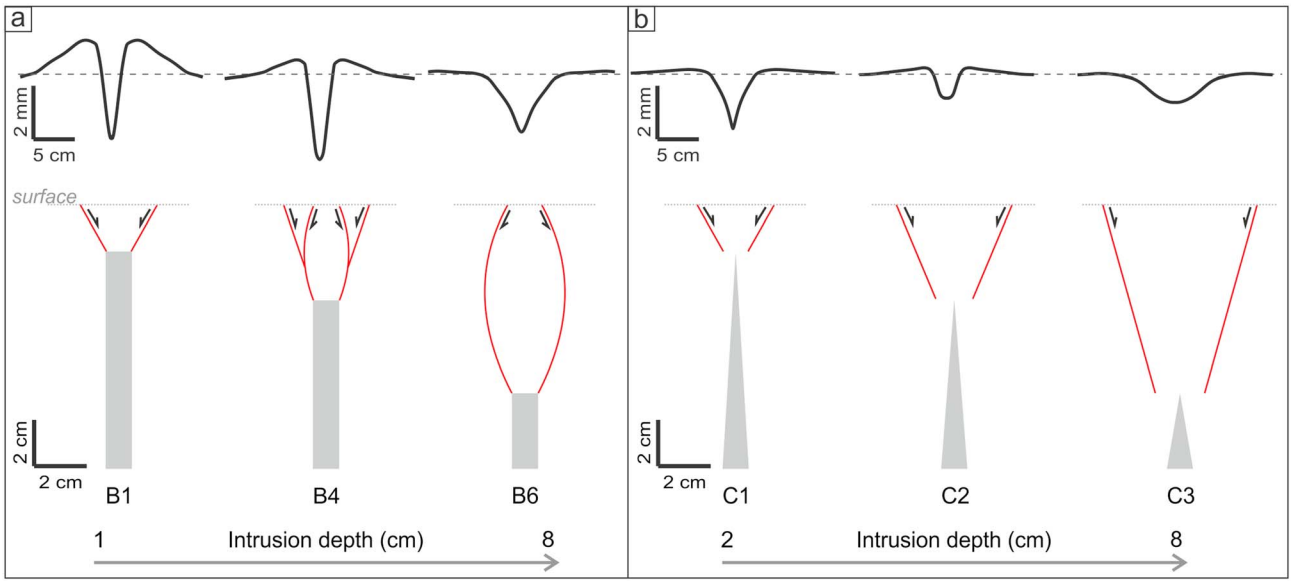

Figure 10. Scheme of the fault patterns at depth (below) and of the vertical displacement profiles at the surface (above) obtained in (a) setup B and (b) setup C. The scale of the profiles is different from that of the fault patterns. Labels below each model refer to Table 1.

In order to better investigate the conditions leading to the nucleation of the normal faults, we calculate the 2-D Coulomb failure stress change on optimally oriented faults due to a vertical opening fracture, simulating a dike, in a homogeneous elastic medium [*Okada*, 1992]. The fracture is composed of 10 × 6 rectangular dislocations at the center, on which a uniform pressure of 5 MPa is applied. The Coulomb stress change is highest at the upper tip of the opening fracture (Figure 13a). However, due to the effect of the free surface, two minor areas with relatively high Coulomb stress change (~5 MPa) are visible also close to the surface, to the sides of the fracture (Figure 13a). Failure nucleation at the surface in a homogeneous medium may be favored by the least lithostatic pressure close to the surface. In order to test this possibility, we compute the total Coulomb stress, where the total normal stress is equal to the lithostatic pressure, plus the normal stress change induced by the fracture (Figure 13b). This shows that the likelihood of fault nucleation is highest at the surface in two wide areas at the side of the dike and at the upper tip, reaching ~20 MPa (Figure 13b). Considering that the mathematical singularity at the fracture tip is not realistic, as nonelastic processes will quickly dissipate such high stresses, the Coulomb stress models suggest that normal faulting is enhanced at the surface to the sides of the dike. Therefore, both the throw distribution of the normal faults in the experiments and the Coulomb stress models suggest that the dike-induced high-angle normal faults nucleate close to the surface and propagate downward.

Surface fracturing during a rifting episode has been often associated with upward propagating normal faults that nucleate from the dike tip [*Grant and Kattenhorn*, 2004; *Tentler*, 2005; *Rowland et al.*, 2007]. Our results show that dike emplacement likely induces downward propagating normal faults nucleating at the surface (Figures 12c). This downward propagation of the normal faults is also proposed by previous studies [*Gudmundsson and Backstrom,* 1991; *Forslund and Gudmundsson*, 1992; *Acocella et al.*, 2003]. Moreover, our modeling evidence is consistent with field evidence from eroded portions of rift zones in Iceland, where any direct connection of normal faults from the upper tip of dikes is lacking. Therefore, our experiments provide a possible solution to reconcile these apparent contradictions in the geometric, kinematic, and causal distribution of dikes and normal faults below rift zones.

4.3.2. Arcuate Normal/Reverse Faults

The inner arcuate faults are observed above rectangular intrusive complexes with depth ≥2 cm (models B3, B4, B5, and B6). The fault throws decreasing toward the surface and the peripheral cross sections suggest that these faults propagate upward from the intrusion top (Figures 4i and 4m and Figures 5g and 5i). These faults result from the differential vertical movement (uplift to sides and subsidence above the intrusions) induced by the intrusions. For example, when the faults form in experiment B4, this vertical movement is estimated as ~1 mm at the surface, or ~10% of the thickness of the injected plates. The transition from

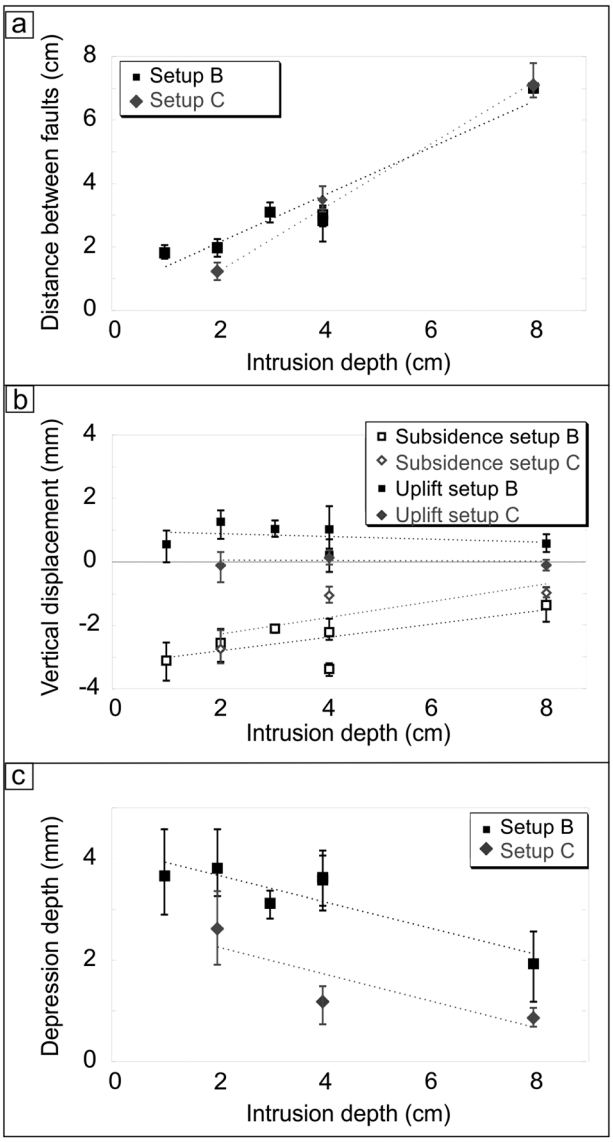

Figure 11. Summary of the data obtained in the nine intrusion models of setups B and C. (a) Mean distance between the conjugate normal faults bordering the graben measured at the surface (the mean distance is extracted from measurements in five cross sections along the graben); (b) absolute vertical displacement at the surface (positive and negative values indicate uplift and subsidence, respectively); (c) variation of the depression depth, that is the sum of the mean subsidence above the intrusion and the mean uplift to the sides.

subsidence to uplift is first accommodated by a broad inward tilt of the surface, subsequently replaced by anelastic deformation; when the arcuate high-angle faults propagate upward, they reach the surface as reverse faults (Figures 12d and 12e). High-angle reverse faults are commonly found with differential vertical movements of adjacent crustal blocks, due to an upward local rotation of the maximum compressive stress, potentially explained by the vault effect above a cavity or, generally speaking, above a subsiding portion of crust. These structures have been observed in sedimentary basins, basement faulting, calderas, and mining cavities [*Wise*, 1963; *Prucha et al.*, 1965; *Given*, 1973; *Vendeville*, 1988; *Roche et al.*, 2000; *Merle et al.*, 2001; *Abe et al.*, 2011]. However, a novelty of our study is that the reverse faults may also result from dike emplacement, not necessarily from the activity of any high-angle dip-slip fault, caldera or mining collapse. While in the latter cases the maximum compressive stress is subvertical at the surface, in our experiments the maximum compressive stress at the upper plate tip is subhorizontal. While approaching the surface, the maximum stress rotates, becoming inward dipping, subvertical, and finally outward dipping, thus explaining the arcuate geometry of the faults (Figure 13c) [i.e., *Patton and Fletcher*, 1995; *Bonafede and Danesi*, 1997]. The absolute (above the intrusions) and relative (on the uplifted portions to the sides of the intrusions) subsidence induced by the intruded plates causes the inward horizontal displacement of the overburden above the intrusions. This develops the outer faults, acting as gravitational structures resulting from the activity of the reverse faults (Figure 12e). The outer normal faults propagate downward, conversely to previous studies on high-angle reverse faults [*Roche et al.*, 2000, and references therein], where they propagate upward. Once the normal outer faults form, they merge along dip with the bottom (inward dipping) portion of the arcuate faults, forming a continuous structure with localized displacement, locking the reverse faults (Figure 12f).

The distinct development of simple graben structures, or arcuate normal/reverse faults, controls also the inside or the outside sense of propagation of the faults at the surface, above the intrusions. In fact, the inside sense of development of the faults is first related to the formation of a graben and then to any other minor normal fault within. Conversely, the outside sense of development of faults is related to the formation of the arcuate faults and then to the normal faults on their hanging wall.

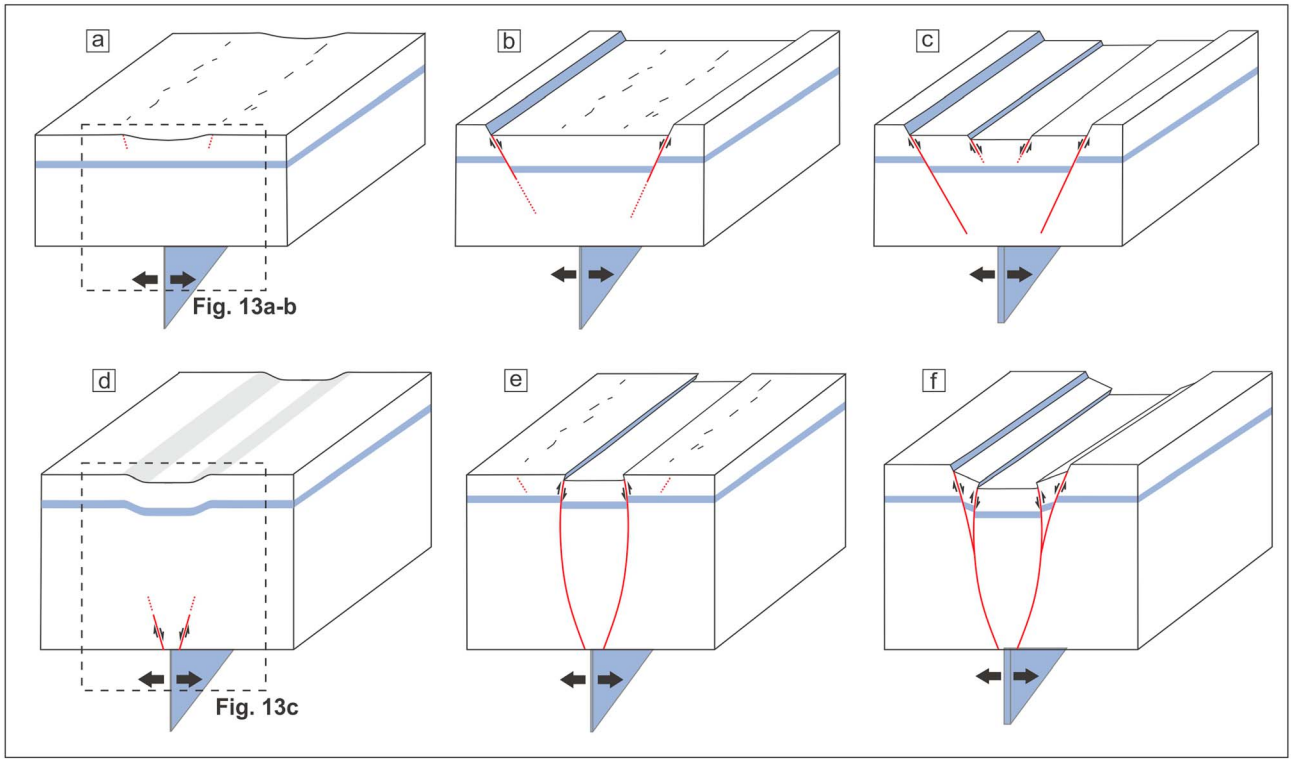

Figure 12. Evolution of the analogue experiments and of the natural prototypes with (a–c) only normal faults and with (d–f) arcuate and normal faults. The development of the downward propagating normal faults is explained in Figures 13a and 13b.

4.4. Comparison to Rift Zones

Here we qualitatively compare the experimental deformation pattern, as derived from the geometry and kinematics of the formed structures, with that observed in nature along rift zones, in order to better define any role of diking. According to the scaling factor used in the experiments, a single plate insertion corresponds to the emplacement of a dike ~10^1 m thick, while the final cumulative thickness at the tip of the intrusive complex is between ~10^2 and ~10^3 m in setup B and between ~10^1 and ~10^2 m in setup C. This implies that the early stage of the models (1–2 inserted plates) can be compared with nature on rifting events or even single rifting episodes, where one or more dikes, for a total thickness of ~10 m, emplace over weeks to a very few years. Alternatively, the final stage of the models can be compared with nature on several rifting episodes, where multiple dikes, for a total thickness of 100 to 1000 m, emplace over centuries or more. The latter condition is, for example, met in the eroded portions of rift zones, as in Eastern Iceland, where the cumulative dike thickness of 10^2–10^3 m (5–10% of fissure swarm width) [*Walker,* 1958, 1960, 1963; *Gudmundsson*, 1983, 1995, and references therein; *Paquet et al.*, 2007] is comparable with the final opening of setup B. In comparing the early stages of setup B to single rifting episodes we have to face a resolution problem: while any structure can be observed in detail on the field, at the experimental scale it can only be appreciated in its very general features above our limit of resolution. This discrepancy may lead to a limited comparison between the details of our experiments and nature. Our early stage experiments will be mainly compared to the 1783–1784 Lakagigar rifting episode (Figure 14), taken here as a representative case of many other rifting episodes (see below); the final stages will be compared to the structure of the mature magmatic systems of Iceland and the Main Ethiopian Rift, also testing the possibility that these may have been produced by several rifting episodes.

4.4.1. Single Rifting Episodes

While the main purpose of this study is to consider the longer-term deformation (~10^2 to ~10^4 years) along magmatic divergent plate boundaries, we first compare the very early stage of deformation of our experiments, obtained inserting 1–2 plates in setup B or up to 20 plates in setup C, with single rifting episodes. This comparison is useful also to have a first qualitative understanding of the structural features

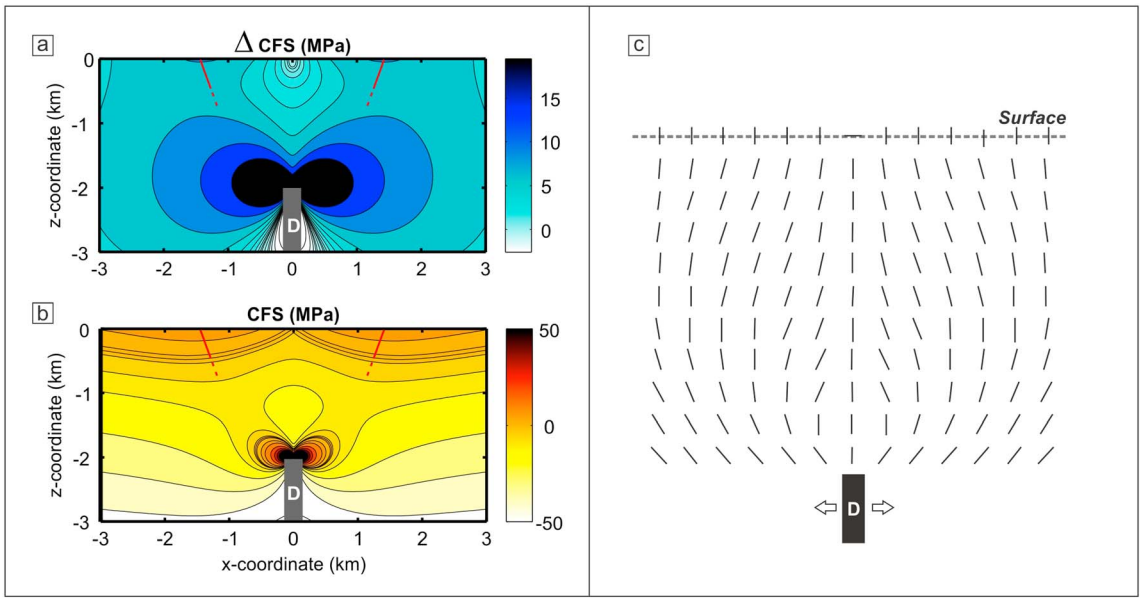

Figure 13. (a) Coulomb stress change on optimally oriented planes induced by an opening fracture simulating the upper portion of a thickening dike complex (*D*, dark gray rectangle) in section view at few km from the surface; (b) total Coulomb stress, where the total normal stress is equal to the lithostatic pressure plus the normal stress change induced by the same fracture of Figure 13a. The stress concentrates at the dike tip, as expected, but also at the surface, where it is large enough to cause faulting. Red lines indicate the downward propagating faults. (c) The development of the arcuate reverse faults depends on the distribution of the maximum compressive stress trajectories induced by an opening dike [after *Patton and Fletcher*, 1995]. See text for details.

and processes involved in the simplest intrusive conditions and, as such, it provides a necessary step to better understand also the longer-term deformation, discussed in section 4.4.2. Single rifting episodes can cause an opening of up to ~10 m at the surface, as at Krafla in 1975–1984, Assal-Ghoubbet in 1973–1979, and Dabbhau in 2005–2010 [*Ruegg et al.*, 1979 ; *Tryggvason*, 1980; *Rubin*, 1992, and references therein; *Wright et al.*, 2006; *Ayele et al.*, 2007; *Grandin et al.*, 2009; *Ebinger et al.*, 2010]. We mainly focus on the 1783–1784 Lakagigar rifting episode, as this occurred in an area which has been undeformed for at least 10 ka, so that the visible surface deformation can be entirely related to the emplacement of the 1783–1784 dike(s) [*Thordarson and Self*, 1993]. The rifting episode along the 27 km long Lakagigar eruptive fissure consisted of ~10 intrusive events. The NE-SW trending fissure comes out in a nearly flat area, locally intersecting the ~200 m higher and older Laki hyaloclastite hill [i.e., *Thordarson and Self*, 1993, and references therein]. The fissure is partly bounded by conjugate normal faults with mean dip of 70° and maximum throw up to 6–10 m, forming a 150 to 450 m wide graben. The fissure is partly interrupted in correspondence to Laki. Here even though the normal faults decrease their vertical displacement, they climb the hill, becoming ~700–800 m distant. Considering the mean fault dip and width of the graben north and south of Laki, we suggest a mean depth d of the intrusion top of ~400 m to the NE and SW sides of the hill (with $d = 1/2w \tan\alpha$, where d is the intrusion depth, w is the graben width, and α is the fault dip). This depth refers to the top of the dike at the moment of faulting the surface; the dike has then subsequently risen, reaching the surface and erupting.

The overall faulting pattern is similar to that obtained in the early stage models of setup B (<5 plates intruded) or final stage models of setup C (20 plates intruded). Similar to Lakagigar, the B1 and C1 models show a narrow graben at the surface bordered by inward dipping normal faults (Figures 3, 6, and 13b). Model C1, with the 3 cm high sand cone above the intrusion, also allows us to simulate the effect of diking on a topography of 10^2 to 10^3 m, similar to Laki. In C1, the constant distance between the faults in the flat area (1.2 cm) is more than doubled in correspondence with the cone (2.8 cm), similar to what is observed at Laki (Figures 6d and 13c). This comparison indicates that a graben widens when developing on a relief; this is due to the locally increased distance between the dike tip and the surface, so that the deeper the dike, the wider the graben. While the graben structure is well developed on Laki, the fissure becomes interrupted, with minor vents on the NW portion of the hill. Laki provides therefore an interesting example of how dike-

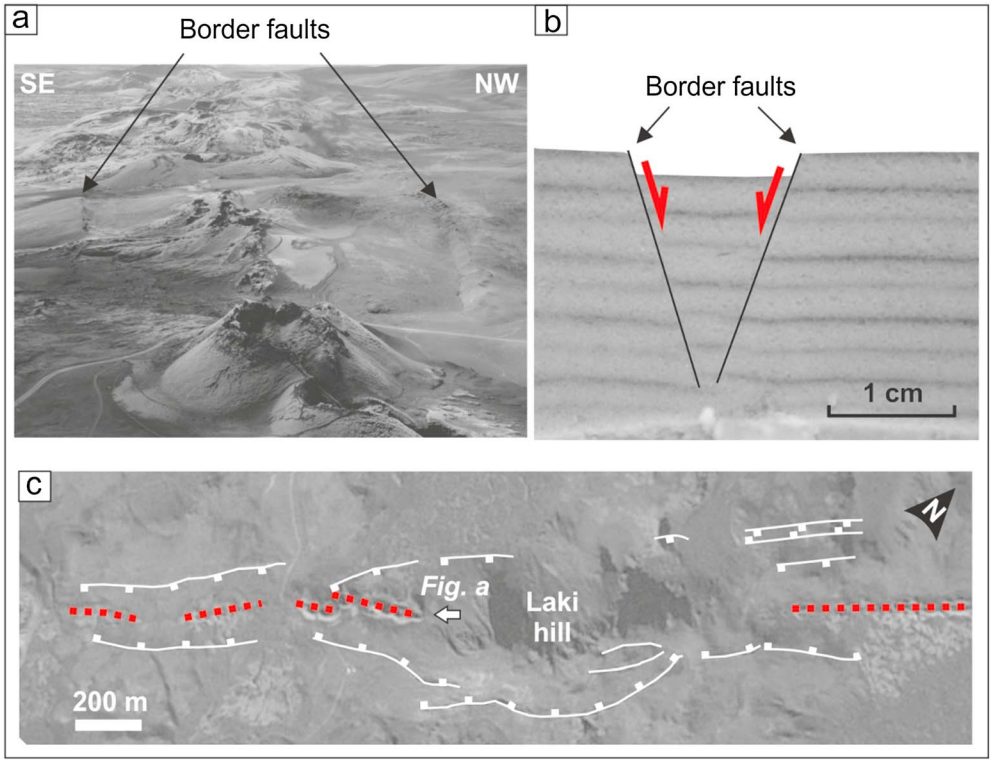

Figure 14. Comparison between experiment C1 and the 1783–1784 Lakagigar eruptive fissure. (a) Panoramic view of the central Lakagigar fissure and its border faults, as seen from Laki hill southward; (b) cross section of experiment C1; (c) map view of the central Lakagigar fissure extracted from Google Earth; the general crater alignment (red dashed lines) and the two border faults (solid lines) are outlined.

induced deformation may be approximated by a graben structure with inward dipping normal faults and this may be eventually influenced by a relief, so that an eruptive fissure may be locally interrupted. Similar to Lakagigar, graben formation has been also repeatedly observed during different rifting episodes or events. The most notable examples include Krafla in 1975–1984, Iceland [*Sigurdsson*, 1980]; Dabbahu in 2005, Afar [i.e., *Rowland et al.*, 2007]; Harrat Lunayyir in 2009, Saudi Arabia [*Pallister et al.*, 2010]; and the more recent Barðarbunga in 2014, Iceland [*Sigmundsson et al.*, 2014; *Ruch et al.*, 2015], highlighting an overall similar deformation pattern to our experiments.

4.4.2. Multiple Rifting Episodes

The final stages of setup B experiments (intrusion of 20 plates with rectangular intrusive complex in section view) can be compared to magmatic systems along divergent plate boundaries undergoing repeated rifting episodes. In particular, here we mainly refer to the well-developed Krafla magmatic system, in the Northern Volcanic Zone of Iceland.

The experiments show an overall symmetric depression bounded by normal faults, similar to the graben-like structures commonly observed in nature. As anticipated, a minor difference is related to the fact that rift zones in nature may not simply consist of a single symmetric graben, but of asymmetric and/or multiple and nested grabens. This is, for example, the case of the Krafla magmatic system: at the surface, its central portion consists of a 2–3 km wide graben, with several normal faults within, defining 30–300 m wide minor nested grabens (Figure 15a) [*Opheim and Gudmundsson*, 1989]. The border faults are usually vertical at the surface, showing the highest displacements of several tens of meters and a tensile area of several meters between the footwall and hanging wall; the footwall layering is usually subhorizontal, whereas the hanging wall layering may be subhorizontal or 20°–30° inward tilted (Figure 15) [*Opheim and Gudmundsson*, 1989; *Angelier et al.*, 1997]. Seismic tomography at Krafla shows that the depth to the top of the high velocity layer varies along the strike of the magmatic system, being shallower (~2–3 km deep) at the center and deepening (~6–7 km deep) toward the northern and southern peripheries (Figure 15b) [*Brandsdóttir et al.*, 1997]. This

suggests a deeper location of the intrusive complex beneath the northern and southern terminations of the magmatic system.

Our models suggest that the overall deformation pattern depends on the depth of the intrusion with respect to the thickness of the dike complex. The shallower intrusion experiment B1 shows that similar to the central portion of the Krafla magmatic system, the graben is delimited by two inward dipping normal faults in which most of the deformation focuses, with minor faults and fractures within (Figures 15c and 15h). The deeper intrusion experiments of setup B also show inner arcuate faults with a reverse kinematics in their upper portion, leading to contraction close to the surface (i.e., experiment B5 in Figure 15i). At Krafla, similar contractional structures are found at the base of the tilted hanging wall of the normal faults several kilometers north of the caldera and, more extensively, at the southern tip of the magmatic system (Figure 15a) [*Trippanera et al.*, 2014], where the intrusive complex appears deeper [*Brandsdóttir et al.*, 1997], even though any possible evaluation of this depth remains highly speculative. An example of contraction at the surface is observed along the 2 km long Grjotagja fault, in the Myvatn area (Figures 15a and 15d–15f). The fault displays 5–6 m of vertical throw with well-defined titled hanging wall, separated from the footwall by a 2 m open fracture (Figure 15d). The contraction at the base of the titled hanging wall exhibits a 1 m wide cylindrical-like fold, whose axis is parallel to the fault strike (Figures 15e and 15f). Similar contractional structures have been also observed at Vogar (Reykjanes Peninsula, Iceland) and Fantale magmatic systems (Main Ethiopian Rift) [*Trippanera et al.*, 2014]. Contractional structures are thus present in various rift systems. The rift segments of Vogar and Fantale currently undergo a lower amount of extension (~6 mm/yr), much lower than that along the central portion of Krafla, of 22–24 mm/yr [*Perlt and Heinert*, 2006]. As the depth to the axial melt zone along divergent plate boundaries is usually proportional to the extension rate [*Purdy et al.*, 1992; *Biggs et al.*, 2009], both the Vogar and Fantale rift segments probably have a deeper intrusive complex than the central portion of the more active and extending Krafla system. At Vogar, the possibility of a deeper intrusive complex is also supported by the dominant eruptive fissures and absence of polygenic volcanoes, suggesting the lack of evident and stable shallow magma chambers [*Gee et al.*, 2000]. In synthesis, it appears that the contractional structures found at the surface in poorly extending (Fantale) and magmatically immature (Vogar) systems, or at the periphery of more developed systems (Krafla), may be the expression of a deeper dike complex, similar to what is observed in setup B experiments. This suggests that any diffuse contraction along divergent plate boundaries may largely depend upon the mean depth of the dike complex and/or the amount of opening of the rift segment. These cases allow a qualitative estimate of the geometric and kinematic boundary conditions for the formation of contractional structures along rifts. In order to try to be more quantitative, we refer to the results of analogue models showing that contractional structures may form when the intrusions are at least 3 cm depth. This means that to develop contractional structure in nature, the minimum depth of the dike complex should be of 300–3000 m. However, our models show that asymmetries in the graben structure may occur, as in B5 (Figure 15i): here the border faults on one side of the graben consist of an inner arcuate and an outer normal fault (as expected for this intrusion depth) and, on the other side, of a single high angle normal fault with negligible hanging wall tilt (Figure 15h). This indicates that normal faults without any contraction may be also found where the dike complex is expected to be relatively deep, as at Reykjanes (Figure 15g). More in general, this suggests that depending on the overall rift structure, contractional structures and hanging wall tilt may not be a rule in rifts with deeper intrusion.

4.4.3. Intrusion Depth Versus Thickness

To better understand how the interplay between the intrusions thickness and depth influences the deformation, we compare the depth to thickness ratio (D/T) of the intrusion in the models and in nature.

In the models, the estimate of the D/T ratio is based on the thickness of the intrusive complex reached when the faults first appear at the surface (Table 1). The D/T is overall constant (always on the order of ~10^1), resulting in a linear trend for each setup (Figure 16a). In particular, the D/T value is ~20 in setup B (rectangular) and ~ 40 in setup C (triangular). These results are obtained with similar boundary conditions in the experiments (including homogenous sand, without layering, and preexisting fractures), so that the difference in D/T between the two setups is only due to the different shape of the intrusive complex; this highlights that surface fracturing occurs inserting fewer plates for setup C (triangular intrusion) than in B (rectangular intrusion), for the same depths of intrusion. This may have two explanations. In the deeper intrusion experiments ($D > 3$ cm), the earliest faults in setup B propagate at depth from the intrusion tip and rise as inner reverse faults, whereas in setup C the earliest faults directly nucleate at the surface as normal faults. For the shallower experiments ($D < 3$ cm), where the earliest faults develop from the surface as normal in both setups, the

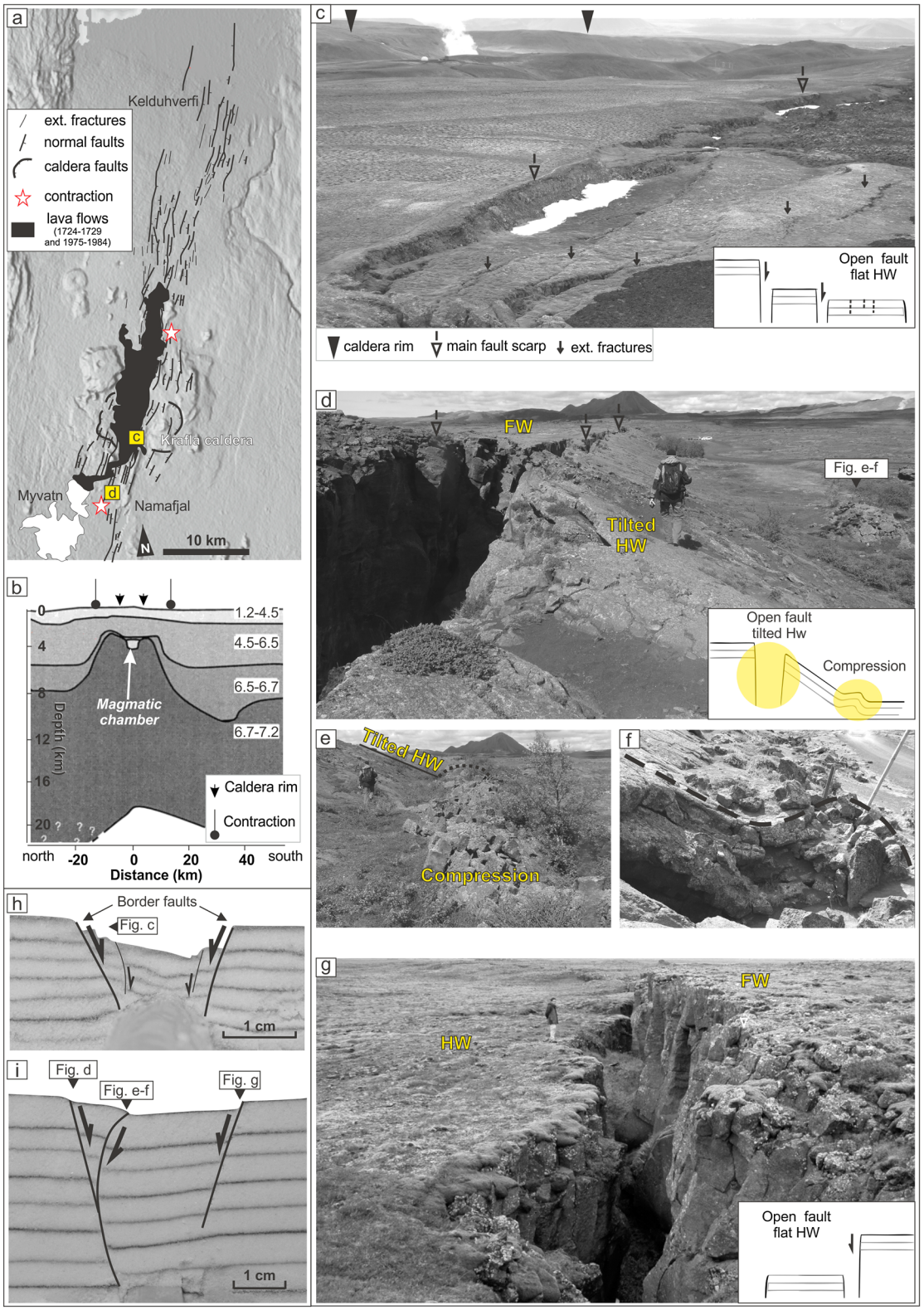

Figure 15. Comparison between experiments and mature rift zones. (a) Map of the Krafla fissure swarm, after *Opheim and Gudmundsson* [1989]. (b) Two-dimensional, compressional velocity model derived from travel time data along the Krafla magmatic system [*Brandsdóttir et al.*, 1997]; velocities are in km/s. Panoramic view and schematic section of (c) fault and tension fractures within the Krafla caldera; (d) the Grjotagja fault to the south of Krafla, showing a tilted hanging wall and basal contraction; location in Figure 15a. (e and f) Contractional structure parallel to the Grjotagja normal fault. (g) View and schematic section of an open normal fault with horizontal hanging wall at Reykjanes, southern Iceland. (h) Cross sections of experiments B1 and (i) B5.

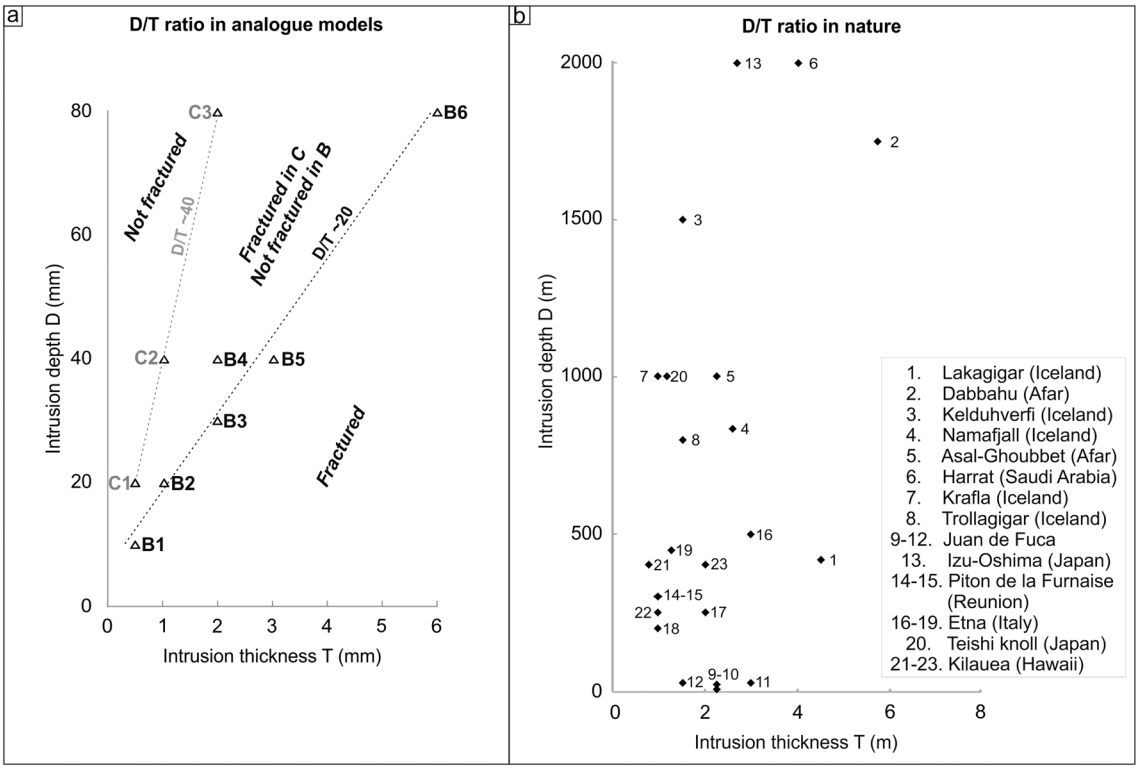

Figure 16. (a) Plot of the dike thickness versus depth when faults appear at surface in the experiments with setup B (black) and C (gray); the relative fitting lines are also shown. (b) Plot of the dike thickness versus depth during diking episodes in which new faults formed at the surface. References: (1 and 8) *Jónsson et al.* (1997), (2) *Wright et al.* (2006), (3) *Sigurdsson* (1980), *Rubin* (1992), (4) *Rubin* (1992), (5) *Stein* (1991), (6) *Pallister et al.* (2010), (7) *Tryggvason* (1980), (9, 10, 11, and 12) *Chadwick and Embley* (1998), (13, 14, 15, 17, 18, 19, 20, and 23) *Dvorak and Dzurisin* (1997), and references therein, (16) *Acocella and Neri* (2003), and (21 and 22) *Pollard et al.* (1983).

highest *D*/*T* ratio for setup C is explained by the increased thickness of the dike complex below its tip, which promotes earlier surface deformation.

The *D*/*T* analysis also suggests that the intrusion shape not only controls the pattern and magnitude of the deformation at the surface (see section 4.2), but it also affects the possibility to develop faults. A smaller *D*/*T* value (~5) at the moment of faulting was obtained by *Mastin and Pollard* [1988] using a mix of sugar and flour, instead of sand, to simulate the host rock. This suggests that the *D*/*T* ratio in analogue models may be affected by boundary conditions (i.e., analogue host rock materials and layering). Despite these variations, there is an overall proportion between the depth to the top of the dikes and their thickness, suggesting that the deeper is a dike, the thicker this has to be in order to fracture the surface.

The mean depth to the top of the dikes and their thickness along divergent plate boundaries and volcanic rift zones, where fault formation or reactivation have been observed, are summarized in Figure 16b [*Tryggvason*, 1980; *Pollard et al.*, 1983; *Stein*, 1991; *Rubin*, 1992; *Jónsson et al.*, 1997; *Dvorak and Dzurisin*, 1997, and references therein; *Chadwick and Embley*, 1998; *Pallister et al.*, 2010; *Acocella and Neri*, 2003; *Wright et al.*, 2006]. The estimated *D*/*T* for these natural cases is highly variable (from ~10^1 to ~10^3) (Figure 16b). This higher variability of *D*/*T* in nature may depend on the nonhomogenous boundary conditions, including variations in the elastic properties of the host rock, layering (i.e., stress barriers due to stiffness contrast between layers), the direction of dike propagation (see end of section 2.3), and the presence of country rock between the dikes of the intrusive complex (septa) and preexisting fractures. The latter may be particularly important, since the presence of faults affects the final surface deformation (Figure 8). Moreover, fault reactivation requires lower energy than fault formation [e.g., *Ranalli*, 1995], suggesting that thinner or deeper dikes may easily reactivate preexisting structures. There are several examples of well-constrained reactivated normal faults during dike emplacement, as at Bárðarbunga in 2014 (Iceland [*Ruch et al.*, 2015]), Dabbahu in 2005 (Afar [*Rowland et al.*, 2007]), Dallol in 2004 (Afar [*Nobile et al.*, 2012]), Lake Natron in 2007 (Tanzania [*Biggs et al.*, 2009]), Sveinagja in 1872–1875 (Iceland [*Gudmundsson and Backstrom*, 1991]), Eldja in 933–941 AD

(Iceland [*Thordarson et al.*, 2001]). In addition, the variability of *D*/*T* may depend upon the uncertainty in estimating the intrusion thickness and depth in nature, as for instance at Lakagigar and Trollagigar. In synthesis, the *D*/*T* values from the analogue models and nature highlight a significant variability, probably reflecting different boundary conditions, as host rock properties and shape of the intrusions. Future and more detailed investigations may allow better capturing these relationships.

This study has shown several consistencies between our dike experiments and the overall structure of divergent plate boundaries, at various scales, from the single diking episode to the entire portion of a rift zone. The fact that most of the structure of a rift, at various scales, can be explained by repeated dike injections highlights the importance of diking in constraining the surface deformation and thus in shaping the structure and topography of divergent plate boundaries. Regional extension is certainly important for the long-term evolution of a divergent plate boundary, providing the required conditions for the rise and emplacement of magma at various levels; it probably also plays an important role, through fault activity and seismicity, during inter-rifting events. However, our results suggest that most, if not all, of the deformation patterns along divergent plate boundaries may be acquired through repeated dike injection, not requiring any direct tectonic contribute (i.e. a magmatic faulting), so that rifting may be approximated by multiple diking episodes.

5. Conclusions

1. Experiments from setup A create a doming delimited by reverse faults, with a secondary apical graben. In experiments with setups B and C, a depression flanked by two uplifted areas is bordered by inward dipping normal faults propagating downward and, for deeper intrusions in B, also by inner faults, reverse at the surface.
2. The comparison between models and nature reveals that setups B and C realistically simulate dike emplacement in the upper crust, conversely to the less realistic setup A. The comparison between these setups confirms that the propagation of a dike consists of the indefinite repetition of two essential steps: (a) initial development of a mode I fracture at the dike tip and (b) lateral opening of the fracture by magma intrusion (as simulated in setups B and C), without any translation of the host rock in the direction of dike propagation (as in setup A).
3. The elastic and anelastic components of surface deformation shown by experiments of setups B and C are consistent with the elastic component suggested by numerical models and the anelastic component shown by geodetic data during rifting events in nature, respectively.
4. The magnitude and pattern of the deformation in the experiments, both at depth and at the surface, depend on depth to the top of the intrusion. The most striking difference is that in setup B shallower intrusions promote normal faults propagating downward, whereas deeper intrusions also promote faults propagating upward becoming reverse close to the surface.
5. While we confirm that dikes may generate normal faults, we also show that the latter propagate from the surface downward. This explains the common lack of any geometric connection between the base of normal faults and the upper tips of dikes in the eroded portions of rift zones, as in Iceland.
6. There is a close similarity between our experiments and divergent plate boundaries, at various scales. The deformation pattern observed in the early stages of our setups B and C, where a graben formed by normal faults forms above the dike(s), is consistent with that during single rifting episodes (i.e., Lakagigar, Iceland). In addition, the final stages of setup B display a graben structure bounded by outer inward dipping normal faults (for shallower dikes), and also with inner arcuate reverse faults (for deeper dikes), similar to what is observed along rift segments in Iceland and the MER. In particular, the deeper intrusions of setup B allow us to explain the formation of the contractional structures observed at the base of the tilted hanging wall along poorly extending rift segments (Fantale, MER), at times lacking a proper shallow magma chamber (Vogar, Iceland) and at the periphery of more active rift segments (as Grjotagja, Krafla, Iceland). Both nature and models suggest that this contraction develops above a deeper dike complex (at least ~10^2 m deep).
7. The onset of formation of the faults at the surface during dike injections depends upon the depth to the top of the dikes *D* and its thickness *T*. There is an overall proportion between the depth to the top of the dike**s** and their thickness in experiments, suggesting that the deeper are the dikes, the thicker they have to be in order to fracture the surface. In the experiments, dike-induced faulting at the surface occurs when *D*/*T* ~20 for rectangular and ~40 for triangular intrusions. However, natural data show no correlation and a higher variability of the *D*/*T* ratios. The discrepancy between models and nature may be mostly attributable to the different boundary conditions (host rocks materials, layering, prefracturation, etc.).

8. The fact that most of the structure of a rift, at various scales, can be explained by repeated dike injections highlights the importance of diking in constraining the surface deformation and thus in shaping divergent plate boundaries. Despite the importance of regional tectonics, our results suggest that most, if not all, of the deformation pattern along divergent plate boundaries may be ultimately acquired through repeated dike intrusions, so that rifting may be approximated by multiple diking episodes.

Acknowledgments
Andrea Giordano helped in the setting up of the experiments. The reviewers Agust Gudmundsson and Thierry Menand provided useful comments, which greatly improved the study. Financed with PRIN 2009 funds (2009H37M59, responsible V. Acocella). Any user can access the data of this work by contacting the corresponding author. ER received funding from the European Union through the ERC Starting Grant project CCMP-POMPEI, grant N. 240583.

References

Abdelmalak, M. M., R. Mourgues, O. Galland, and D. Bureau (2012), Fracture mode analysis and related surface deformation during dyke intrusion: Results from 2D experimental modelling, *Earth Planet. Sci. Lett.*, *359–360*, 93–105, doi:10.1016/j.epsl.2012.10.008.

Abe, S., H. van Gent, and J. L. Urai (2011), DEM simulation of normal faults in cohesive materials, *Tectonophysics*, *512*(1–4), 12–21, doi:10.1016/j.tecto.2011.09.008.

Acocella, V., and M. Neri (2003), What makes flank eruprions? The 2001 Etna eruption and its possible triggering mechanisms, *Bull. Volcanol.*, *65*, 517–529, doi:10.1007/s00445-003-0280-3.

Acocella, V., and M. Neri (2009), Dike propagation in volcanic edifices: Overview and possible developments, *Tectonophysics*, *471*(1–2), 67–77, doi:10.1016/j.tecto.2008.10.002.

Acocella, V., F. Cifelli, and R. Funiciello (2001), The control of overburden thickness on resurgent domes: Insights from analogue models, *J. Volcanol. Geotherm. Res.*, *111*(1–4), 137–153.

Acocella, V., T. Korme, and F. Salvini (2003), Formation of normal faults along the axial zone of the Ethiopian Rift, *J. Struct. Geol.*, *25*, 503–513.

Adam, J., J. L. Urai, B. Wieneke, O. Oncken, K. Pfeiffer, N. Kukowski, J. Lohrmann, S. Hoth, W. van der Zee, and J. Schmatz (2005), Shear localisation and strain distribution during tectonic faulting—New insights from granular-flow experiments and high-resolution optical image correlation techniques, *J. Struct. Geol.*, *27*, 283–301, doi:10.1016/j.jsg.2004.08.008.

Angelier, J., F. Bergerat, O. Dauteuil, and T. Villemin (1997), Effective tension-shear relationships in extensional fissure swarms, axial rift zone of northeastern Iceland, *J. Struct. Geol.*, *19*(5), 673–685, doi:10.1016/S0191-8141(96)00106-X.

Ayele, A., E. Jacques, M. Kassim, T. Kidane, A. Omar, S. Tait, and G. King (2007), The volcano–seismic crisis in Afar, Ethiopia, starting September 2005, *Earth Planet. Sci. Lett.*, *255*(1–2), 177–187, doi:10.1016/j.epsl.2006.12.014.

Biggs, J., F. Amelung, N. Gourmelen, T. H. Dixon, and S.-W. Kim (2009), InSAR observations of 2007 Tanzania rifting episode reveal mixed fault and dyke extension in an immature continental rift, *Geophys. J. Int.*, *179*(1), 549–558, doi:10.1111/j.1365-246X.2009.04262.x.

Bjornsson, A., K. Saemundsson, P. Einarsson, E. Tryggvason, and K. Gronvold (1977), Current rifting episode in north Iceland, *Nature*, *266*, 318–322.

Bonaccorso, A. (2003), Dynamics of the December 2002 flank failure and tsunami at Stromboli volcano inferred by volcanological and geophysical observations, *Geophys. Res. Lett.*, *30*(18), 1941, doi:10.1029/2003GL017702.

Bonafede, M., and S. Danesi (1997), Near-field modifications of stress induced by dyke injection at shallow depth, *Geophys. J. Int.*, *130*(2), 435–448, doi:10.1111/j.1365-246X.1997.tb05659.x.

Brandsdóttir, B., W. H. Menke, P. Einarsson, R. S. White, and R. K. Staples (1997), Faroe-Iceland Ridge Experiment. 2. Crustal structure of the Krafla central volcano, *J. Geophys. Res.*, *102*(B4), 7867–7886, doi:10.1029/96JB03799.

Buck, W. R., P. Einarsson, and B. Brandsdóttir (2006), Tectonic stress and magma chamber size as controls on dike propagation: Constraints from the 1975–1984 Krafla rifting episode, *J. Geophys. Res.*, *111*, B12404, doi:10.1029/2005JB003879.

Calais, E., N. d'Oreye, J. Albaric, A. Deschamps, D. Delvaux, J. Déverchère, and C. Wauthier (2008), Strain accommodation by slow slip and dyking in a youthful continental rift, East Africa, *Nature*, *456*(7223), 783–7, doi:10.1038/nature07478.

Cervelli, P., P. Segall, K. Johnson, M. Lisowski, and A. Miklius (2002), Sudden aseismic fault slip on the south flank of Kilauea volcano, *Nature*, *415*(6875), 1014–1018, doi:10.1038/4151014a.

Chadwick, W. W., and R. W. Embley (1998), Graben formation associated with recent dike intrusions and volcanic eruptions on the mid-ocean ridge, *J. Geophys. Res.*, *103*, 9807–9825, doi:10.1029/97JB02485.

Dieterich, J. H., and R. W. Decker (1975), Finite element modelling of surface deformation associated with volcanism, *J. Geophys. Res.*, *80*(29), 4094–4102, doi:10.1029/JB080i029p04094.

Dvorak, J. A., and D. Dzurisin (1997), Volcano geodesy: The research for magma reservoirs and the formation of eruptive vents, *Rev. Geophys.*, *35*(3), 343–384, doi:10.1029/97RG00070.

Dzurisin, D. (2006), *Volcano Deformation: Geodetic Monitoring Techniques*, edited by P. Blondel, 441 pp., Springer, Berlin.

Ebinger, C., A. Ayele, D. Keir, J. V. Rowland, G. Yirgu, T. Wright, and I. Hamling (2010), Length and timescales of rift faulting and magma intrusion: The Afar rifting cycle from 2005 to present, *Annu. Rev. Earth Planet. Sci.*, *38*, 439–466, doi:10.1146/annurev-earth-040809-152333.

Fink, H. H., and D. D. Pollard (1983), Structural evidence of dikes beneath silicic domes, Medicine Lake Highland Volcano, California, *Geology*, *11*, 458–461.

Forslund, T., and A. Gudmundsson (1991), Crustal spreading due to dikes and faults in SW island, *J. Struct. Geol.*, *13*(4), 443–457.

Forslund, T., and A. Gudmundsson (1992), Structure of Tertiary and Pleistocene normal faults in Iceland, *Tectonics*, *11*, 57–68, doi:10.1029/91TC01536.

Gee, M. A. M., R. N. Taylor, M. F. Thirlwall, and B. J. Murton (2000), Axial magma reservoirs located by variation in lava chemistry along Iceland's mid-ocean ridge, *Geology*, *28*, 699–702, doi:10.1130/0091-7613(2000)28<699.

Given, I. A. (Ed.) (1973), *Mining Engineering Handbook*, Part City Press, New York.

Grandin, R., A. Socquet, R. Binet, Y. Klinger, E. Jacques, J.-B. de Chabalier, and P. Pinzuti (2009), September 2005 Manda Hararo-Dabbahu rifting event, Afar (Ethiopia): Constraints provided by geodetic data, *J. Geophys. Res.*, *114*, 1–20, doi:10.1029/2008JB005843.

Grant, J. V., and S. A. Kattenhorn (2004), Evolution of vertical faults at an extensional plate boundary, southwest Iceland, *J. Struct. Geol.*, *26*, 537–557, doi:10.1016/j.jsg.2003.07.003.

Gudmundsson, A. (1983), Form and dimensions of dykes in eastern Iceland, *Tectonophysics*, *95*, 295–307.

Gudmundsson, A. (1995), Infrastructure and mechanics of volcanic systems in Iceland, *J. Volcanol. Geotherm. Res.*, *64*, 1–22.

Gudmundsson, A. (2003), Surface stresses associated with arrested dykes in rift zones, *Bull. Volcanol.*, *65*, 606–619.

Gudmundsson, A. (2006), How local stresses control magma-chamber ruptures, dyke injections, and eruptions in composite volcanoes, *Earth Sci. Rev.*, *79*, 1–31.

Gudmundsson, A., and K. Backstrom (1991), Structure and development of the Sveinagja graben, Northeast Iceland, *Tectonophysics*, *200*, 111–125.

Gudmundsson, A., and I. F. Loetveit (2005), Dyke emplacement in a layered and faulted rift zone, *J. Volcanol. Geotherm. Res.*, *144*, 311–327.

Jónsson, S., P. Einarsson, and F. Sigmundsson (1997), Extension across a divergent plate boundary, the Eastern Volcanic Rift Zone, south Iceland, 1967–1994, observed with GPS and electronic distance measurements, *J. Geophys. Res.*, *102*(B6), 11,913–11,929, doi:10.1029/96JB03893.

Jónsson, S., H. Zebker, P. Cervelli, P. Segall, H. Garbeil, P. Mouginis-mark, and S. Rowland (1999), A shallow-dipping dike fed the 1995 flank eruption at Fernandina Volcano, Galàpagos, observed by satellite radar interferometry, *Geophys. Res. Lett.*, *26*(8), 1077–1080, doi:10.1029/1999GL900108.

Keir, D., I. J. Hamling, A. Ayele, E. Calais, C. Ebinger, T. J. Wright, and L. Bennati (2009), Evidence for focused magmatic accretion at segment centers from lateral dike injections captured beneath the Red Sea rift in Afar, *Geology*, *37*(1), 59–62, doi:10.1130/G25147A.1.

Mastin, L. G., and D. D. Pollard (1988), Surface deformation and shallow dike intrusion processes at Inyo Craters, Long Valley, California, *J. Geophys. Res.*, *93*(B11), 13,221–13,235, doi:10.1029/JB093iB11p13221.

Mathieu, L., B. van Wyk de Vries, E. P. Holohan, and V. R. Troll (2008), Dykes, cups, saucers and sills: Analogue experiments on magma intrusion into brittle rocks, *Earth Planet. Sci. Lett.*, *271*(1–4), 1–13, doi:10.1016/j.epsl.2008.02.020.

Merle, O., N. Vidal, and B. van Wyk de Vries (2001), Experiments on vertical basement fault reactivation below volcanoes, *J. Geophys. Res.*, *106*(B2), 2153–2162, doi:10.1029/2000JB900352.

Nobile, A., C. Pagli, D. Keir, T. J. Wright, A. Ayele, J. Ruch, and V. Acocella (2012), Dike-fault interaction during the 2004 Dallol intrusion at the northern edge of the Erta Ale Ridge (Afar, Ethiopia), *Geophys. Res. Lett.*, *39*, 1–6, doi:10.1029/2012GL053152.

Norini, G., and V. Acocella (2011), Analogue modeling of flank instability at Mount Etna: Understanding the driving factors, *J. Geophys. Res.*, *116*, B07206, doi:10.1029/2011JB008216.

Okada, Y. (1992), Internal deformation due to shear and tensile faults in a half-space, *Bull. Seismol. Soc. Am.*, *82*(2), 1018–1040.

Opheim, J. A., and A. Gudmundsson (1989), Formation and geometry of fractures, and related volcanism, of the Krafla fissure swarm, northeast Iceland, *Geol. Soc. Am. Bull.*, *101*(12), 1608–1622, doi:10.1130/0016-7606(1989)101<1608.

Pallister, J. S., et al. (2010), Broad accommodation of rift-related extension recorder by dyke intrusion in Saudi Arabia, *Nat. Geosci.*, *3*(10), 708–712, doi:10.1038/ngeo966.

Panien, M., G. Schreurs, and A. Pfiffner (2006), Mechanical behaviour of granular materials used in analogue modelling: Insights from grain characterisation, ring-shear tests and analogue experiments, *J. Struct. Geol.*, *28*(9), 1710–1724, doi:10.1016/j.jsg.2006.05.004.

Paquet, F., O. Dauteuil, E. Hallot, and F. Moreau (2007), Tectonics and magma dynamics coupling in a dyke swarm of Iceland, *J. Struct. Geol.*, *29*(9), 1477–1493, doi:10.1016/j.jsg.2007.06.001.

Patton, T. L., and R. C. Fletcher (1995), Mathematical block-motion model for deformation of a layer above a buried fault of arbitrary dip and sense of slip, *J. Struct. Geol.*, *17*(10), 1455–1472, doi:10.1016/0191-8141(95)00034-B.

Perlt, J., and M. Heinert (2006), Kinematic model of the South Icelandic tectonic system, *Geophys. J. Int.*, *164*(1), 168–175, doi:10.1111/j.1365-246X.2005.02795.x.

Philipp, S. L., F. Afşar, and A. Gudmundsson (2013), Effects of mechanical layering on hydrofracture emplacement and fluid transport in reservoirs, *Front. Earth Sci.*, *1*, 4, doi:10.3389/feart.2013.00004.

Pollard, D. D. (1987), Elementary fracture mechanics applied to the structural interpretation of dykes, in *Mafic Dyke Swarms*, *Geol. Assoc. Can. Spec. Pap.*, vol. 34, edited by H. C. Halls and W. F. Fahrig, pp. 5–24.

Pollard, D. D., and G. Holzhausen (1979), On the mechanical interaction between a fluid-filled fracture and the Earth's surface, *Tectonophysics*, *53*, 27–57.

Pollard, D. D., P. T. Delaney, W. A. Duffield, E. T. Endo, and A. T. Okamura (1983), Surface deformation in volcanic rift zones, *Tectonophysics*, *94*, 541–584.

Prucha, J. J., J. A. Graham, and R. P. Nickelsen (1965), Basement-controlled deformation in Wyoming province of Rocky Mountains foreland, *Am. Assoc. Petrol. Géol. Bull.*, *49*, 966–992.

Purdy, G. M., L. S. L. Kong, G. L. Christeson, and S. C. Solomon (1992), Relationship between spreading rate and seismic structure of mid-ocean ridges, *Lett. Nat.*, *355*, 815–817.

Ranalli, G. (1995), *Rheology of the Earth*, Chapman and Hall, London.

Roche, O., T. H. Druitt, and O. Merle (2000), Experimental study of caldera formation, *J. Geophys. Res.*, *105*(B1), 395–416, doi:10.1029/1999JB900298.

Rowland, J. V., E. Baker, C. J. Ebinger, D. Keir, T. Kidane, J. Biggs, and T. J. Wright (2007), Fault growth at a nascent slow-spreading ridge: 2005 Dabbahu rifting episode, Afar, *Geophys. J. Int.*, *171*(3), 1226–1246, doi:10.1111/j.1365-246X.2007.03584.x.

Rubin, A. M. (1992), Dike-induced faulting and graben subsidence in volcanic rift zones, *J. Geophys. Res.*, *97*(B2), 1839–1858, doi:10.1029/91JB02170.

Rubin, A. M., and D. D. Pollard (1988), Dike-induced faulting in rift zones of Iceland and Afar, *Geology*, *16*, 413–417.

Ruch, J., V. Acocella, N. Geshi, A. Nobile, and F. Corbi (2012), Kinematic analysis of vertical collapse on volcanoes using experimental models time series, *J. Geophys. Res.*, *117*, B07301, doi:10.1029/2012JB009229.

Ruch, J., S. Jónsson, T. Wang, W. Xu, and D. Trippanera (2015), Graben formation during the Bárðarbunga rifting event in central Iceland. Geophysical Research Abstract, 17, EGU2015-12247, EGU General Assembly 2015.

Ruegg, J. C., J. C. Lépine, and A. Tarantola (1979), Geodetic measurements of rifting associated with a seismo-volcanic crisis in Afar, *Geophys. Res. Lett.*, *6*(11), 817–820, doi:10.1029/GL006i011p00817.

Sigmundsson, F., et al. (2014), Segmented lateral dyke growth in a rifting event at Barðarbunga volcanic system, Iceland, *Nature*, doi:10.1038/nature14111.

Sigurdsson, O. (1980), Surface deformation of the Krafla fissure swarm in two rifting events, *J. Geophys.*, *47*, 154–159.

Stein, R. S. (1991), Contemporary, Holocene, and Quaternary deformation of the Asal Rift, Djibouti: Implications for the mechanics of slow spreading ridges, *J. Geophys. Res.*, *96*(B13), 21,789–21,806, doi:10.1029/91JB02118.

Swanson, B. D. A., W. A. Duffield, and R. Fiske (1976), Displacement of the south flank of Kilauea Volcano: The result of forceful intrusion of magma into the rift zones, *Geol. Surv. Prof. Pap.*, *963*, 1–39.

Tentler, T. (2005), Propagation of brittle failure triggered by magma in Iceland, *Tectonophysics*, *406*(1–2), 17–38, doi:10.1016/j.tecto.2005.05.016.

Thordarson, T., and S. Self (1993), The Laki (Skaftlir Fires) and Grimsvotn eruptions in 1783–1785, *Bull. Volcanol.*, *55*, 233–263.

Thordarson, T., D. J. Miller, G. Larsen, S. Self, and H. Sigurdsson (2001), New 947 estimates of sulfur degassing and atmospheric mass-loading by the 934 AD Eldjá eruption, 948 Iceland, *J. Volcanol. Geotherm. Res.*, *108*, 33–54, doi:10.1016/S0377-0273(00)00277-8.

Trippanera, D., V. Acocella, and J. Ruch (2014), Dike-induced contraction along oceanic and continental divergent plate boundaries, *Geophys. Res. Lett.*, *40*, 1–7, doi:10.1002/2014GL061570.

Tryggvason, E. (1980), Subsidence events in the Krafla area, North Iceland, 1975–1979, *J. Geophys.*, *47*, 141–153.

Vendeville, B. (1988), Modèles expérimentaux de fracturation de la couverture contrôlée par des failles normales dans le socle, *C. R. Acad. Sci. Paris, Sér. II*, *307*, 1013–1019.

Walker, G. P. L. (1958), Geology of the Reydarfjordur Area, Eastern Iceland, *Q. J. Geol. Soc.*, *114*(1–4), 367–391, doi:10.1144/gsjgs.114.1.0367.

Walker, G. P. L. (1960), Zeolite zones and dike distribution in relation to the structure of the basalts of Eastern Iceland, *J. Geol. Soc. (London)*, *68*, 515–527.

Walker, G. P. L. (1963), The Breiddalur central volcano, eastern Iceland, *Q. J. Geol. Soc.*, *119*(1–4), 29–63, doi:10.1144/gsjgs.119.1.0029.

Westergaard, H. M. (1939), Bearing pressures and cracks, *Trans. Am. Soc. Mech. Eng.*, *61*, A49–A53.

Wise, D. U. (1963), Keystone faulting and gravity sliding driven by basement uplift of Owl Creek Mountains, Wyoming, *Am. Assoc. Pet. Geol. Bull.*, *47*, 586–596.

Wright, T. J., C. Ebinger, J. Biggs, A. Ayele, G. Yirgu, D. Keir, and A. Stork (2006), Magma-maintained rift segmentation at continental rupture in the 2005 Afar dyking episode, *Nature*, *442*, 291–294, doi:10.1038/nature04978.